

Supermassive Black Holes with High Accretion Rates in Active Galactic Nuclei. VIII. Structure of the Broad-Line Region and Mass of the Central Black Hole in Mrk 142*

YAN-RONG LI,¹ YU-YANG SONGSHENG,¹ JIE QIU,¹ CHEN HU,¹ PU DU,¹ KAI-XING LU,² YING-KE HUANG,¹ JIN-MING BAI,²
WEI-HAO BIAN,³ YE-FEI YUAN,⁴ LUIS C. HO,^{5,6} AND JIAN-MIN WANG^{1,7,8}
(SEAMBH COLLABORATION)

¹Key Laboratory for Particle Astrophysics, Institute of High Energy Physics, Chinese Academy of Sciences, 19B Yuquan Road, Beijing 100049, China

²Yunnan Observatories, Chinese Academy of Sciences, Kunming 650011, China

³Physics Department, Nanjing Normal University, Nanjing 210097, China

⁴Department of Astronomy, University of Science and Technology of China, Hefei 230026, China

⁵Kavli Institute for Astronomy and Astrophysics, Peking University, Beijing 100871, China

⁶Department of Astronomy, School of Physics, Peking University, Beijing 100871, China

⁷National Astronomical Observatories of China, Chinese Academy of Sciences, 20A Datun Road, Beijing 100012, China

⁸School of Astronomy and Space Science, University of Chinese Academy of Sciences, 19A Yuquan Road, Beijing 100049, China

ABSTRACT

This is the eighth in a series of papers reporting on a large reverberation mapping campaign to measure black hole (BH) mass in high accretion rate active galactic nuclei (AGNs). We employ the recently developed dynamical modeling approach for broad-line regions (BLRs) based on the method of Pancoast et al. to analyze the reverberation mapping dataset of Mrk 142 observed in the first monitoring season. In this approach, continuum variations are reconstructed using a damped random walk process, and BLR structure is delineated using a flexible disk-like geometry, in which BLR clouds move around the central BH with Keplerian orbits or inflow/outflow motion. The approach also includes the possibilities of anisotropic emission of BLR clouds, non-linear response of the line emission to the continuum, and different long-term trends in the continuum and emission-line variations. We implement the approach in a Bayesian framework that is apt for parallel computation and use a Markov Chain Monte Carlo technique to recover the parameters and uncertainties for the modeling, including mass of the central BH. We apply three BLR models with different prescriptions of BLR clouds distributions and find that the best model for fitting the data of Mrk 142 is a two-zone BLR model, consistent with the theoretical BLR model surrounding slim accretion disks. The best model yields a BH mass of $\log(M_{\bullet}/M_{\odot}) = 6.23^{+0.26}_{-0.45}$, resulting in a virial factor of $\log f = -0.36^{+0.33}_{-0.54}$ for the full width at half maximum of the H β line measured from the mean spectrum. The virial factors for the other measures of the H β line width are also presented.

Keywords: black hole physics — galaxies: active — galaxies: individual (Mrk 142) — quasars: general

1. INTRODUCTION

Broad emission lines with widths of several thousands of kilometers per second are a hallmark feature of the spectra of active galactic nuclei (AGNs). The basic photoionization theory and the long-known fact that both the lines and continuum emissions of AGNs vary on quite short timescales, ranging from days to months (e.g., Burbidge 1967; Cromwell & Weymann 1970), spurred the proposal of the widely used technique “reverberation mapping” (RM) by Blandford & McKee (1982). The principle underlying RM is that the broad-line region (BLR) is photoionized by the central ion-

izing continuum stemmed from the accretion disk and reproduces broad emission lines. The temporal behaviors of emission lines are thereby blurred echoes of continuum variations with light-crossing delays. The responses from different parts of the BLR have different time delays and Doppler shifting velocities due to the motion of BLR gas in the gravitational potential well of the central black hole (BH). Thus, by appropriately analyzing the variation properties of continuum and emission lines, one can place constraints on the geometry and kinematics of the BLR as well as the BH mass.

Due to the insufficient cadences or signal-to-noise ratios of spectroscopic data, the major goals of most early RM experiments have largely focused on measuring characteristic time lags between the variations of emission lines and continuum, which correspond to the light-travel distance from the continuum source to the line-emitting gas. The measured time lags are thereby used to deduce the sizes of BLRs (e.g., Peter-

liyanrong@mail.ihep.ac.cn, wangjm@mail.ihep.ac.cn

* The software developed in this work is available at <https://github.com/LiyraAstrroph/BRAINS>.

son 1993). The recognition that emission-line lags and line widths follow the “virial relationship” lends RM technique to be a promising method for measuring BH mass in AGNs (e.g., Wandel 1997; Ho 1999; Peterson & Wandel 1999; Peterson et al. 2004). Specifically, based on the virial theorem, virial BH mass measurements are generally derived by combining the emission-line lags (τ) and line widths (ΔV) using a simple recipe (e.g., Peterson et al. 2004)

$$M_{\text{vir}} = f \frac{c\tau(\Delta V)^2}{G}, \quad (1)$$

where c is the speed of light and G is the gravitational constant. To connect this virial mass with true BH mass, a virial factor f has to be invoked on account of our ignorance of the geometry and kinematic of BLRs. The virial factor is practically calibrated by comparing RM AGNs with measured bulge stellar velocity dispersion against the well established $M_{\bullet} - \sigma_{\star}$ relation of local quiescent galaxies (e.g., Onken et al. 2004; Ho & Kim 2014). Clearly, the virial factor determined in this way applies in a statistical sense and is subject to the intrinsic scatter of the $M_{\bullet} - \sigma_{\star}$ relation, which is about 0.3 dex (e.g., Kormendy & Ho 2013). It is unknown yet if the virial factor has a common value for various AGN populations. Given the complicated structures of BLRs inferred from the previous velocity-binned RMs (e.g., Bentz et al. 2010; Denney et al. 2010; Grier et al. 2013b; Du et al. 2016b, hereafter Paper VI), the virial factor is most likely to vary from object to object. Recent recalibration of the virial factor by Ho & Kim (2014) using the comprehensively revised $M_{\bullet} - \sigma_{\star}$ relation of Kormendy & Ho (2013) indeed showed that the virial factor seems to depend on the bulge type (classical or pseudo) of the host galaxies. Therefore, invoking of the virial factor in traditional RM approach actually impedes on its own a further improvement on BH mass measurements (Krolik 2001).

The way around this weakness of traditional RM approach is, similar to the BH mass measurements in quiescent galaxies through stellar or gas dynamics, to develop feasible dynamical models for BLRs and analyze velocity-resolved RM data to determine the BH mass self-consistently without the need to invoke the virial factor. Such an approach dates back to the early work of Bottorff et al. (1997) who applied the outflow model of Emmering et al. (1992) to the RM database of the well-monitored Seyfert galaxy NGC 5548, in an attempt to constrain the central BH mass and the BLR dynamics. With the aid of the development of the mathematical description of AGN variability (Kelly et al. 2009), Pancoast et al. (2011) constructed a Bayesian framework with a flexible BLR dynamical model for RM data analysis. In this new approach, BH mass and other BLR parameters (e.g., inclination angle and opening angle) are fully determined by comparing the model predictions with the observed time series of continuum and broad emission lines. Pancoast et al. (2014a) subsequently reinforced their previous framework by incorporating more complicated phenomenological treatments on the anisotropy of BLR emissions and inflows and outflows. Based on the model of Pancoast et al. (2011), Li et al. (2013)

also carried out an independent implementation that, additionally, includes the non-linear response of emission lines to the ionizing continuum. Although the dynamical modeling approach is still at its early stage, the application to several RM AGNs shows its remarkable capability for understanding BLR dynamics and measuring BH mass (Brewer et al. 2011b; Pancoast et al. 2012, 2014b; Grier et al. 2017; Pancoast et al. 2018; Williams et al. 2018).

In 2012, we began a large RM observational project using the Lijiang 2.4m telescope at Yunnan Observatories, aiming at monitoring a sample of selected high-accretion-rate AGN (hereafter dubbed as super-Eddington accreting massive black hole; SEAMBH) candidates with good cadences for measuring reliably BH mass and studying BLR physics. In particular, based on slim accretion disk model that describes BH accretion at high accretion rates, Wang et al. (2014b) demonstrated that the geometrically thick funnel of inner slim disk produce anisotropic radiation field, which divides the surrounding BLR into two regions with distinct incident ionizing photon fluxes. Such BLR structures are different from these of sub-Eddington accreting BHs, which are powered by standard geometrically thin accretion disks (Shakura & Sunyaev 1973). By combining with the previous RM sample that mainly consists of sub-Eddington accreting AGNs (Bentz et al. 2013), this RM project provides important complementary objects to generate a homogeneous sample with a broad range of accretion rates.

The project has continued uninterrupted for six years and is still ongoing. In the first monitoring season (2012–2013), nine objects are finally verified to show statistically significant $H\beta$ lags through cross-correlation analysis. The resulting datasets and time-lag analysis between the optical continuum and $H\beta$ emission line and Fe II emission have been reported in the papers of this series Du et al. (2014, Paper I), Wang et al. (2014a, Paper II), Hu et al. (2015, Paper III), and Xiao et al. (2018, Paper VII). The datasets and time-lag measurements from the other monitoring seasons have also been reported in the papers of this series Du et al. (2015, Paper IV), Du et al. (2016a, Paper V), and Du et al. (2018, Paper IX). We make use of the spectroscopic datasets for the nine objects in the first monitoring season and employ our developed dynamical modeling for BLRs to study the structure and dynamics of the $H\beta$ BLRs and derive the BH mass for these nine objects. This paper reports the first application to Mrk 142, which has the highest data quality among the nine objects.

The paper is organized as follows. We briefly describe the properties of observation data for Mrk 142 in Section 2. Section 3 describes the method for reconstruction of the continuum light curve and Section 4 presents the methodology for BLR dynamical modeling and the Bayesian framework for inferring the model parameters. Section 5 summarizes the results from the dynamical modeling including the obtained BH mass, and also compares our results with these from the cross-correlation analysis. The discussions and conclusions are given in Sections 6 and 7, respectively.

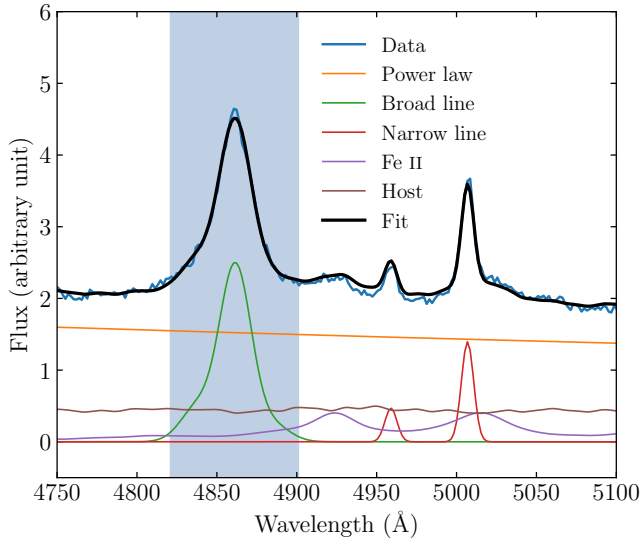


Figure 1. An example of spectral decomposition for Mrk 142. Shaded area indicates the wavelength range used in our BLR modeling.

2. OBSERVATION DATA

Mrk 142 was spectroscopically and photometrically monitored between October 2012 and June 2013. The details of the observations and data reduction and analysis were presented in [Paper I](#) and [Paper III](#). All the spectra were taken by simultaneously placing a nearby comparison star in the slit to achieve high-accuracy flux calibration. Since the host galaxies are extended and resolved, this observing strategy can, however, result in apparent flux variations of the host galaxy contamination due to variable seeing and miscentering. A spectral decomposition scheme as described below helps to alleviate this effect (see Appendix A of [Paper III](#)).

To isolate the AGN continuum and $H\beta$ line, a spectral decomposition was performed by including a featureless AGN power-law continuum, Fe II blends, various emission lines ($H\beta$, [O III], He II, He I, and several coronal lines), and a host galaxy template (see [Paper III](#) for details). The Fe II blends were fitted by the template from [Boroson & Green \(1992\)](#) and the host galaxy template was chosen to be a single stellar population model with an instantaneous burst of 11 Gyr and a metallicity of $Z = 0.05$. The AGN continuum flux was measured as the flux at 5100 Å from the decomposed featureless power-law component. The $H\beta$ line profile is obtained by subtracting the above-listed components from each spectrum. The narrow $H\beta$ line component, which originates from the narrow-line region, is not subtracted because of two reasons: first, Mrk 142 has fairly weak narrow [O III] lines, indicating that the narrow $H\beta$ lines are also weak; second, the spectral resolution is about 500 km s⁻¹ in terms of the full width at half maximum (FWHM), too low to reliably decompose the narrow component ([Paper III](#)). [Figure 1](#) shows an example of spectral decomposition of an individual-night spectrum for Mrk 142. [Paper III](#) also presented the $H\beta$ lag with respect to

Table 1. Properties of the observation data of Mrk 142.

	Value	Unit
(1) z	0.0449	...
(2) Dates	273-413	day
(3) N_{con}	101	...
(4) $N_{H\beta}$	101	...
(5) $F_{\text{var}}(5100\text{\AA})$	10.0%	...
(6) $F_{\text{var}}(H\beta)$	6.8%	...
(7) $\text{FWHM}_{\text{mean}}(H\beta)$	1588 ± 58	km s ⁻¹
(8) $\sigma_{\text{mean}}(H\beta)$	972 ± 12	km s ⁻¹
(9) $\text{FWHM}_{\text{rms}}(H\beta)$	1663 ± 86	km s ⁻¹
(10) $\sigma_{\text{rms}}(H\beta)$	1130 ± 12	km s ⁻¹
(11) $\Delta\lambda_{\text{dis}}$	240 ± 34	km s ⁻¹
(12) $\lambda(H\beta)$	4821-4901	Å
(13) τ_{cent}	$7.9^{+1.2}_{-1.1}$	day
(14) $\log(M_{\bullet}/M_{\odot})$	$6.59^{+0.07}_{-0.07}$...

NOTE—The table rows are as follows: (1) redshift, (2) date range, JD-2,456,000, (3) number of epochs in the 5100 Å continuum light curve, (4) number of epochs of spectroscopy, (5) variability characteristic F_{var} of the 5100 Å continuum, (6) variability characteristic F_{var} of the $H\beta$ fluxes, (7) $H\beta$ FWHM measured from the mean spectrum, (8) $H\beta$ line dispersion measured from the mean spectrum, (9) $H\beta$ FWHM measured from the RMS spectrum, (10) $H\beta$ line dispersion measured from the RMS spectrum, (11) spectral resolution given in terms of dispersion, (12) $H\beta$ wavelength range, set to be about three times the $H\beta$ FWHM, (13) $H\beta$ centroid time lag in the rest frame measured from CCF analysis by [Paper III](#), and (14) BH mass, calculated using the centroid time lag and $H\beta$ FWHM measured from the mean spectrum with a virial factor $f_{\text{mean,FWHM}} = 1$.

the 5100 Å continuum through the cross-correlation method. [Table 1](#) lists the overall properties of the observation data of Mrk 142.

Three points merit emphasis regarding the datasets used for our dynamical modeling. First, the spectra are aligned using [O III] $\lambda 5007$ as the wavelength reference to correct the night-to-night wavelength shifts. Second, the wavelength range of the $H\beta$ line is adopted to be about three times the FWHM. Third, by comparing the observed spectrum of the comparison stars with stellar templates, [Du et al. \(2016b\)](#) determined the spectral resolution of the spectra at each individual epoch. We use the mean values for Mrk 142 as the input of the instrumental resolution to our dynamical modeling procedure (see below).

To correct for the redshift effect, we reduce the observation dates of the series by a factor $(1+z)$, where $z = 0.0449$ is the redshift of Mrk 142. Since the analysis only depends on the time differences between data points rather than the absolute times, this manipulation equivalently converts the time series to the rest frame.

3. CONTINUUM MODELING

We use the damped random walk (DRW) model to describe the variability of the continuum fluxes (e.g., [Kelly et al. 2009](#); [Zu et al. 2013](#) and references therein), which allows us to interpolate and extrapolate continuum light curve in a statistical way ([Pancoast et al. 2011](#)). In the DRW model, the

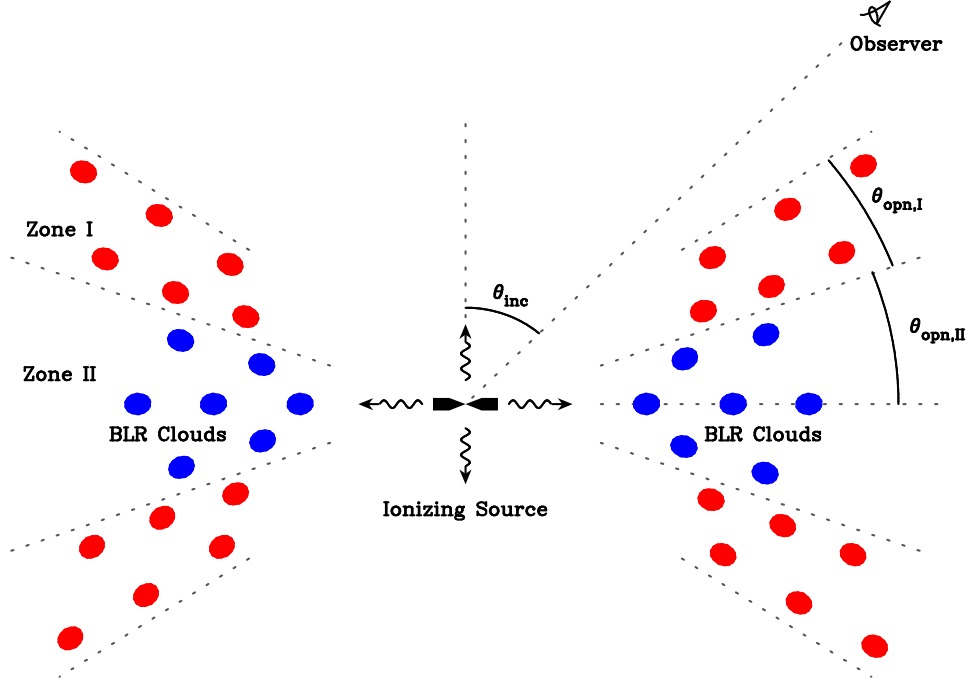


Figure 2. Schematic of BLR model *M3*. *M3* is a two-zone model with the basic scenario that at high accretion rate regime, the geometrically thick funnel of the inner region of slim disks produces anisotropic ionizing radiation field that leads to two distinct BLR zones I and II. We also construct two additional BLR models *M1* and *M2*, which have the same disk-like geometry as zone II in model *M3* (see Section 4 for details).

covariance function between any two points at time t_1 and t_2 is given by

$$S(t_1, t_2) = \sigma_d^2 \exp\left(-\frac{|t_1 - t_2|}{\tau_d}\right), \quad (2)$$

where σ_d is the long-term standard deviation of the variation and τ_d is the typical timescale of variation. In this prescription, the variation of light curves at short time scale ($t \ll \tau_d$) is $\sigma\sqrt{t}/2\tau_d$. To relax the correlation between σ_d and τ_d , a new parameterization of $\hat{\sigma}_d = \sigma_d/\sqrt{\tau_d}$ is used to replace σ_d .

Let s denote the real underlying signal of the continuum variations to be inferred from observations. A set of measurements y_c for a continuum light curve in a monitoring campaign can be written as

$$y_c = s + Lq + n_c, \quad (3)$$

where n_c represents the measurement noises and the term Lq represents a linearly varying trend in the light curve. Here L is a matrix of known coefficients and q is a vector of unknown linear coefficients (see Rybicki & Press 1992 for details). Assuming that the measurement noise n_c is Gaussian and uncorrelated, the likelihood probability for y_c is (Rybicki & Press 1992; Li et al. 2013)

$$P(y_c | \sigma_d, \tau_d, q) = \frac{1}{\sqrt{(2\pi)^m |C|}} \exp\left(-\frac{(y_c - Lq)^T C^{-1} (y_c - Lq)}{2}\right), \quad (4)$$

where superscript “ T ” denotes the transposition, m is the number of data points, $C = S + N$, S is the covariance matrix

of s given by Equation (2), and N is the covariance matrix of n_c . In our calculations, we by default include the zero-order linear trend. In this case, L is a vector with all unity elements and q is the long-term mean value of the light curve. This helps to remove the bias in modeling the light curve at epochs far from any data points (see discussion in Rybicki & Press 1992).

Given parameters (σ_d, τ_d, q) , the probability of a signal s underlying a set of measurements y_c is (e.g., Rybicki & Press 1992; Zu et al. 2011)

$$P(s | y_c) \propto \exp\left[-\frac{(s - \hat{s})^T Q^{-1} (s - \hat{s})}{2} - \frac{(q - \hat{q})^T C_q^{-1} (q - \hat{q})}{2} - \frac{(y_c - L\hat{q})^T C^{-1} (y_c - L\hat{q})}{2}\right], \quad (5)$$

where

$$\hat{s} = SC^{-1}(y_c - Lq), \quad (6)$$

$$\hat{q} = C_q L^T C^{-1} y_c, \quad (7)$$

$$C_q = (L^T C^{-1} L)^{-1}, \quad (8)$$

$$Q = [S^{-1} + N^{-1}]^{-1}. \quad (9)$$

Equation (5) indicates that the signal s is a Gaussian process with mean \hat{s} and covariance matrix Q (Rybicki & Press 1992). One can thereby generate a signal s by adding to \hat{s} a Gaussian process with zero mean and covariance matrix Q given by Equation (9). Similarly, the probability of q is a Gaussian with mean \hat{q} and covariance matrix C_q . As a result, a typical realization for the observed continuum light curve

Table 2. Parameters for models *M1*, *M2*, and *M3*.

Parameter	Model ^a	Prior	Range	Unit	Implication
Continuum					
$\hat{\sigma}_d$	<i>M1, M2, M3</i>	Logarithmic	$(10^{-3}, 10^{-1})$...	Long-term standard deviation of DRW variation
τ_d	<i>M1, M2, M3</i>	Logarithmic	$(1, 10^4)$	Day	Typical timescale of DRW variation
\mathbf{u}_q	<i>M1, M2, M3</i>	Gaussian	Deviations of long-term trend of continuum fluxes
\mathbf{u}_s	<i>M1, M2, M3</i>	Gaussian	Deviations of continuum light curve
BLR					
<i>A</i>	<i>M1, M2, M3</i>	Logarithmic	(0.1, 10)	...	Response coefficient of BLR
δ	<i>M1, M2, M3</i>	Uniform	(-1, 3)	...	Power-law index for non-linear response of BLR
μ	<i>M1, M3</i>	Logarithmic	(0.1, 100)	ld	Mean radius of BLR
β	<i>M1, M3</i>	Uniform	(0, 2)	...	Shape of radial distribution of BLR particles
<i>F</i>	<i>M1, M3</i>	Uniform	(0, 1)	...	Inner edge of BLR
μ_I	<i>M3</i>	Logarithmic	(0.1, 100)	ld	Mean radius of BLR region I
β_I	<i>M3</i>	Uniform	(0, 2)	...	Shape of radial distribution of BLR particles for region I
F_I	<i>M3</i>	Uniform	(0, 1)	...	Inner edge of BLR region I
ρ_I	<i>M3</i>	Uniform	(0, 1)	...	Fraction of BLR particles in region I
α	<i>M2</i>	Uniform	(1, 3)	...	Slope of double power law of radial distribution of BLR particles
R_0	<i>M2</i>	Logarithmic	(0.1, 100)	ld	characteristic radius of double power law
F_{in}	<i>M2</i>	Uniform	(0, 1)	...	Inner radius of double power law
F_{out}	<i>M2</i>	Logarithmic	(1, 10)	...	Outer radius of double power law
θ_{inc}	<i>M1, M2, M3</i>	Uniform	(0, 90)	Degree	Inclination angle of BLR to the light of sight
θ_{opn}	<i>M1, M2, M3</i>	Uniform	(0, 90)	Degree	Opening angle of BLR
$\theta_{opn, I}$	<i>M3</i>	Uniform	(0, 90)	Degree	Opening angle of BLR region I
κ	<i>M1, M2, M3</i>	Uniform	(-0.5, 0.5)	...	Anisotropy of particle emission
γ	<i>M1, M2, M3</i>	Uniform	(1, 5)	...	Clustering of BLR in the θ direction
ξ	<i>M1, M2, M3</i>	Uniform	(0, 1.5)	...	Transparency of equatorial material
M_\bullet	<i>M1, M2, M3</i>	Logarithmic	$(10^5, 10^9)$	M_\odot	BH mass
f_{ellip}	<i>M1, M2, M3</i>	Uniform	(0, 1)	...	Fraction of bound elliptical orbits
f_{flow}	<i>M1, M2, M3</i>	Uniform	(0, 1)	...	Flag for determining inflowing or outflow orbits
$f_{ellip, I}$	<i>M3</i>	Uniform	(0, 1)	...	Fraction of bound elliptical orbits for region I
$f_{flow, I}$	<i>M3</i>	Uniform	(0, 1)	...	Flag for determining inflowing or outflow orbits for region I
$\sigma_{\rho, circ}$	<i>M1, M2, M3</i>	Logarithmic	(0.001, 0.1)	...	Radial standard deviation around circular orbits
$\sigma_{\Theta, circ}$	<i>M1, M2, M3</i>	Logarithmic	(0.001, 1.0)	...	Angular standard deviation around circular orbits
$\sigma_{\rho, rad}$	<i>M1, M2, M3</i>	Logarithmic	(0.001, 0.1)	...	Radial standard deviation around radial orbits
$\sigma_{\Theta, rad}$	<i>M1, M2, M3</i>	Logarithmic	(0.001, 1.0)	...	Angular standard deviation around radial orbits
θ_e	<i>M1, M2, M3</i>	Uniform	(0, 90)	Degree	Rotation angle of inflow or outflow orbits
σ_{turb}	<i>M1, M2, M3</i>	Logarithmic	(0.001, 0.1)	...	Standard deviation of macroturbulent velocities
α_p	<i>M1, M2, M3</i>	Uniform	(-0.1, 0.1)	...	Slope for different long-term trends in continuum and emission line
$\sigma_{s, l}$	<i>M1, M2, M3</i>	...	(1.0, 10.0)	...	Additive noise for emission line data

NOTE—Parameters in bold are composed of an array. The unit of α_p is (the unit of flux) \times day⁻¹. The prior ranges of *A* and α_p are assigned in terms of the mean fluxes of the light curves normalized to unity. The prior for $\sigma_{s, l}$ is set as $P(x) = 1/(1+x)$, where $x = \sigma_{s, l}/\bar{\sigma}_l$ and $\bar{\sigma}_l$ is the mean measurement error of the emission line. $P(x)$ behaves like a uniform prior when $x \ll 1$ and behaves like a logarithmic prior when $x \gg 1$ (Gregory 2011).

^a This column indicates whether the parameters are included in the three models *M1*, *M2*, and *M3*.

is obtained by

$$\tilde{\mathbf{y}}_c = (\mathbf{u}_s + \hat{\mathbf{s}}) + \mathbf{L}(\mathbf{u}_q + \hat{\mathbf{q}}), \quad (10)$$

where \mathbf{u}_s and \mathbf{u}_q are Gaussian processes with zero mean and covariance matrices \mathbf{Q} and \mathbf{C}_q , respectively. Note that given $(\sigma_d, \tau_d, \mathbf{q})$, $\hat{\mathbf{s}}$ and $\hat{\mathbf{q}}$ are uniquely determined by Equations (6) and (7). In the following analysis, we use \mathbf{u}_s and \mathbf{u}_q as free parameters, which are further constrained by additional measured data of broad emission lines.

4. BLR MODELING

As mentioned above, Pancoast et al. (2011) developed a Bayesian approach for BLR dynamical modeling, which was firstly applied to the RM data of Arp 151 (Brewer et al. 2011b) and Mrk 50 (Pancoast et al. 2012). Li et al. (2013) carried out an independent implementation of this approach by additionally including the non-linear response of the emission lines to the continuum and detrending of light curves. Pancoast et al. (2014a) further improved their BLR model by including more complicated treatments on anisotropy of line emissions and on cloud kinematics so as to generate highly asymmetric line profiles. This improved approach was subsequently applied to several RM objects by Pancoast et

al. (2014b), Grier et al. (2017), Pancoast et al. (2018), and Williams et al. (2018). The BLR models used in this paper are based on Pancoast et al. (2014a) and Li et al. (2013), but with several new modifications. Here, for the sake of completeness, we list all the essential details.

The basic scenario of BLR dynamical modeling is that BLRs are composed of a large number of discrete, point-like clouds, which orbit around the central BH (e.g., Netzer 1990). These clouds are exposed to the central ionizing source and instantaneously re-radiate emission lines by absorbing the ionizing continuum. Due to lacking UV/X-ray monitoring data, we use 5100 Å fluxes as a surrogate for the ionizing continuum. This may lead to the non-linear response of BLR cloud emission (Gaskell & Sparke 1986; Goad & Kozlowski 2014). To avoid confusion, hereafter we use the term “particles” to represent units of emissions from these BLR clouds. The effect of inverse square decline of the incident continuum flux density is assumed to be implicitly included in the radial distribution of BLR particles. Below we construct three BLR models *M1*, *M2*, and *M3*. The first model *M1* is the same as Pancoast et al. (2014a)’s model. *M2* differs from *M1* at the prescription of the radial distributions of BLR particles. *M3* is a two-zone model motivated by the theoretical model of Wang et al. (2014b). Throughout the calculations, a spherical coordinate frame (r, θ, φ) is used and the BH is placed in the origin.

4.1. Geometry

The distribution of BLR particles is assumed to be axisymmetric and follows a flexible disk-like geometry, which can yield a variety of shapes with suitable parameters, including shells, spheres, and rings. The BLR has an inclination angle θ_{inc} to the observer, which is defined by the angle between the line of sight and the symmetric axis of the BLR. The BLR particles subtend an opening angle θ_{opn} , which is defined by $\theta_{\text{opn}} = \pi/2$ for a spherical BLR and $\theta_{\text{opn}} = 0$ for an infinitely thin disk-like BLR (see the schematic Figure 1 of Li et al. 2013). Within the opening angle, particles are distributed uniformly over φ -direction. In θ -direction, particles are distributed with a prescription (Pancoast et al. 2014a)

$$\theta = \cos^{-1} [\cos \theta_{\text{opn}} + (1 - \cos \theta_{\text{opn}}) \times U^\gamma], \quad (11)$$

where U is a random number from a uniform distribution between 0 and 1 and γ is a free parameter that controls the extent to which particles are clustered along the outer face of the BLR disk.

We use two types of radial distribution for BLR particles as follows.

- *M1*: The radial distribution is parameterized by a Gamma distribution, same as in Pancoast et al. 2014a. Specifically, the radial location of a particle is assigned by

$$r = F\mu + (1-F)\mathcal{R}, \quad (12)$$

where \mathcal{R} is a random number drawn from the Gamma distribution with a mean μ and a standard deviation

$\beta\mu^1$, and F is a fraction to account for the possibility that within an inner edge ($F\mu$), clouds are completely ionized so that they do not reverberate to the continuum.

- *M2*: The radial distribution is parameterized by a double power law (Stern et al. 2015) as

$$f(r) \propto \begin{cases} r^\alpha, & \text{for } F_{\text{in}} \leq r/R_0 \leq 1, \\ r^{-\alpha}, & \text{for } 1 \leq r/R_0 \leq F_{\text{out}}, \end{cases} \quad (13)$$

where α is the slope of the power law, R_0 is the characteristic radius, and F_{in} and F_{out} are fractions to describe the inner and outer radius.

Hereafter, we also denote the BLR model with the Gamma distribution as *M1* and with the power-law distribution as *M2*.

4.2. Emissivity

We assume that the ionizing continuum is isotropic, and is proportional to the optical 5100 Å continuum. Self-shadowing among clouds is not considered for the present simple modeling. As in Li et al. (2013), we relax the usual assumption of linear responses of emission lines to the continuum and adopt a power-law index δ to describe the non-linearity as

$$\epsilon(t) \propto f_c^{1+\delta}(t-\tau), \quad (14)$$

where ϵ is the emissivity of the particle at time t irradiated by the ionizing continuum with a flux of f_c at time $t-\tau$.

To account for the possibility that BLR clouds are optically thick so that their emission is anisotropic, we use a simple parameterization by assigning a weight to each particle as (Blandford & McKee 1982)

$$w = \frac{1}{2} + \kappa \cos \phi, \quad (15)$$

where κ is a free factor in the range of $[-1/2, 1/2]$ and ϕ is the angle between the observer’s and particle’s line of sight to the central ionizing source.

It is possible that the particles below the equatorial plane are partially obscured by some material in the equatorial plane. As in Pancoast et al. (2014a), we use a parameter ξ to describe the transparency of this equatorial material. For $\xi \rightarrow 0$, the entire half of the BLR below the equatorial plane is obscured; whereas for $\xi \rightarrow 1$, the half becomes transparent.

4.3. Dynamics

The motion of particles is assumed to be fully dominated by the gravity of the central BH. Following Pancoast et al. (2014a), three kinematic components are considered: bound elliptical orbits, and bound and unbound inflow or outflow. The fraction of bound elliptical orbits is described by a parameter f_{ellip} and the remaining fraction $1 - f_{\text{ellip}}$ of BLR particles is thus either inflowing or outflowing. A parameter

¹ If the Gamma function is parameterized with a shape parameter (a) and a scale parameter (s), they obey the relations $a = 1/\beta^2$ and $s = \beta^2\mu$.

f_{flow} is used to determine whether BLR particles are inflowing ($0 < f_{\text{flow}} < 0.5$) or outflowing ($0.5 < f_{\text{flow}} < 1$).

Velocities of particles are firstly assigned in the particles' orbital planes and then converted into real three-dimension velocities through coordinate rotations. For bound elliptical orbits, radial and tangential velocities are drawn from Gaussian distributions centered around the point $(v_r, v_\phi) = (0, v_{\text{circ}})$ of an ellipse in the $v_r - v_\phi$ plane (see Figure 2 in Pancoast et al. 2014a), where $v_{\text{circ}} = \sqrt{GM_\bullet/r}$. The ellipse has a semiminor axis v_{circ} in the v_ϕ -direction and a semimajor axis $\sqrt{2}v_{\text{circ}}$ in the v_r -direction. The widths of Gaussian distributions for radial and tangential velocities are controlled by parameters $\sigma_{\rho, \text{circ}}$ and $\sigma_{\Theta, \text{circ}}$, respectively, where ρ and Θ are the radial and angular coordinates in the $v_r - v_\phi$ plane.

For inflowing or outflowing particles, velocities are assigned same as for elliptical orbits, except that the Gaussian distributions are centered around points $(v_r, v_\phi) = (\pm\sqrt{2}v_{\text{circ}}, 0)$ in the $v_r - v_\phi$ plane, where “+” corresponds to outflow and “-” corresponds to inflow. In addition, the Gaussian distributions are allowed to rotate along the ellipse by an angle θ_e considering that real clouds may have a combination of Keplerian and inflow/outflow motion. When $\theta_e = 0$, inflowing or outflowing velocities are centered around the escape velocity $v_r = \pm\sqrt{2}v_{\text{circ}}$. As $\theta_e \rightarrow 90^\circ$, inflowing or outflowing particles approach the same motion as the elliptical orbits.

Macroturbulence is included by adding a random velocity to the light-of-sight velocity of particles as (Pancoast et al. 2014a)

$$v_{\text{turb}} = \mathcal{N}(0, \sigma_{\text{turb}})v_{\text{circ}}, \quad (16)$$

where $\mathcal{N}(0, \sigma_{\text{turb}})$ is random number drawn from a Gaussian distribution with a zero mean and standard deviation σ_{turb} .

4.4. A Two-zone BLR Model M3

At high accretion rates, accretion disks are usually categorized into slim disk regime (Abramowicz et al. 1988), which forms a geometrically thick funnel in the inner disks due to the strong radiation pressure. Wang et al. (2014b) showed that the self-shadowing effect of such a funnel feature produces anisotropy of the ionizing radiation field that leads to two distinct BLR regions. Mrk 142 was identified to be an SEAMBH with a dimensionless accretion rate of $\mathcal{M} = 45$ using the BH mass derived from cross-correlation function (CCF) analysis and an assumed inclination angle of $\cos\theta_{\text{inc}} = 0.75$ (Du et al. 2016a), where $\mathcal{M} = \dot{M}c^2/L_{\text{Edd}}$, \dot{M} is mass accretion rate, and L_{Edd} is the Eddington luminosity. Motivated by the above scenario, we construct a two-zone BLR model. Figure 2 shows a schematic of the two-zone BLR geometry for Mrk 142. Zone I is ionized by radiation emitted within the funnel whereas zone II is ionized by radiation emitted outside the funnel. For simplicity, we assume that the ionizing emissions received by zone I and zone II are correlated and we thereby apply the observed 5100 Å continuum light curve for the both regions. In addition, we neglect the obscuration of zone I to zone II.

The configuration of this two-zone model is set as follows. The structure and dynamics of zone I are described with the same parameters as in model M1 in Section 4.1. For zone II, the radial distribution of BLR particles follows a Gamma distribution but with distinct parameters. Meanwhile, zone I also has new dynamical parameters $f_{\text{ellip, I}}$ and $f_{\text{flow, I}}$. Hereafter, we denote this two-zone model as M3. In a nutshell, compared to model M1, M3 has new additional parameters ($\mu_{\text{I}}, \beta_{\text{I}}, F_{\text{I}}, \theta_{\text{opn, I}}, \rho_{\text{I}}, f_{\text{ellip, I}}$, and $f_{\text{flow, I}}$). The meanings of these parameters are also explained in Table 2.

4.5. Different Long-term Trends of Continuum and Emission Line

There is incident detection in previous RM observations that the variations of continuum and emission line undergo different long-term (compared with RM timescales) secular trends (e.g., Denney et al. 2010; Li et al. 2013; Peterson et al. 2014), which are irrelevant to RM analysis and therefore should be appropriately accounted. A low-order polynomial was usually used to detrend the light curves of continuum and emission line (Welsh 1999), which generally leads to improvements in the RM analysis.

In the present framework, we use a linear polynomial to model the difference in the long-term trends of continuum and emission line. We add this linear trend to the reconstructed continuum light curve so that the new light curve has the same secular trend as that of emission line. To keep the mean flux of the continuum light curve unchanged, only a free parameter is needed to delineate the slope the linear polynomial. There are no apparently different trends by visual inspection in the light curves of Mrk 142, therefore we do not include this procedure in our calculations. However, there are indeed a few objects in our monitored sample showing different long-term trends. We describe the procedure for including different long-term trends here for the sake of completeness. We stress that here the linear trend serves the purpose of accounting for the different long-term trends in continuum and emission line, distinguished from the trend defined in Section 3.1, which only refers to the continuum itself.

5. BAYESIAN FRAMEWORK

5.1. Formulations

It is now trivial to calculate the intrinsic emission line profile at time t and velocity v by summing up the emissions from BLR particles with a line-of-sight velocity v

$$f_{i, \text{int}}(v, t) = \sum_i \epsilon_i(v, t) = A \sum_i \delta(v - u_i) w_i f_c^{1+\gamma}(t - \tau_i), \quad (17)$$

where $\delta(x)$ is the Dirac function, A is the response coefficient, and w_i, u_i, r_i , and τ_i are, respectively, the weight of emissivity (given by Equation (15)), the line-of-sight velocity, the distance to the central source, and the time-lag of re-radiation from the i -th particle. The continuum flux f_c includes the different long-term trends in continuum and emission, as described in Section 4.5. Here the subscript “int” refers to in-

trinsic line profile, to distinguish from the observed line profile, which suffers additional broadening due to the seeing and instrument effects. The so-called transfer function reads

$$\Psi_{\text{int}}(v, \tau) = A \sum_i w_i \delta(v - u_i) \delta(\tau - \tau_i). \quad (18)$$

This simplifies Equation (17) into a generalized integral form for RM with a non-linear response,

$$f_{l,\text{int}}(v, t) = \int \Psi_{\text{int}}(v, \tau) f_c^{1+\gamma}(t - \tau) d\tau. \quad (19)$$

For *long* time series, manipulating time averaging upon both sides of the above equation yields the delay integral of $\Psi(v, t)$

$$\Psi_{\text{int}}(v) = \int \Psi_{\text{int}}(v, \tau) d\tau = \frac{\langle f_{l,\text{int}}(v, t) \rangle}{\langle f_c(t) \rangle}, \quad (20)$$

where the angle brackets denote time average. The velocity integral of $\Psi(v, \tau)$,

$$\Psi(\tau) = \Psi_{\text{int}}(\tau) = \int \Psi_{\text{int}}(v, \tau) dv, \quad (21)$$

yields the usual velocity-unresolved delay map.

To mock real observations, we need to take into account line broadening caused by the seeing and instruments. The observed line profile can be deemed to be a convolution between the predicted intrinsic line profile and line-broadening function. Equation (19) is recasted into

$$\begin{aligned} f_l(v, t) &= f_{l,\text{int}}(v, t) \otimes \xi(v, t) \\ &= \int \Psi_{\text{int}}(v, \tau) \otimes \xi(v, t) f_c^{1+\gamma}(t - \tau) d\tau, \end{aligned} \quad (22)$$

where “ \otimes ” denotes a convolution operation over velocity axis and $\xi(v, t)$ is the line-broadening function, which generally depends on the instrument and seeing conditions. We again manipulate time averaging upon both sides of the above equation and note that $\xi(v, t)$ and $f_c(t)$ are usually uncorrelated. For *long* time series, we have

$$\langle f_l(v, t) \rangle = \langle f_c(t) \rangle \int \Psi_{\text{int}}(v, \tau) \otimes \langle \xi(v, t) \rangle d\tau. \quad (23)$$

If we denote

$$\Psi(v) = \int \Psi_{\text{int}}(v, \tau) \otimes \langle \xi(v, t) \rangle d\tau, \quad (24)$$

we obtain exactly the same form for $\Psi(v)$ as Equation (20),

$$\Psi(v) = \frac{\langle f_l(v, t) \rangle}{\langle f_c(t) \rangle} \propto \langle f_l(v, t) \rangle. \quad (25)$$

This implies that the delay integral of (broadened) transfer function has the same shape as the mean observed profile of the emission line (Blandford & McKee 1982; Perry et al. 1994). Unless stated otherwise, transfer functions shown in

figures throughout the paper by default include the broadening effect, namely, convolution with the line-broadening function.

A set of measurements for an emission line in real observations is a sum of the predicted line profiles and measurement noises. Written in a concise form of tensors

$$\mathbf{y}_l = \mathbf{f}_l + \mathbf{n}_l = \mathbf{f}_{l,\text{int}} \otimes \boldsymbol{\xi} + \mathbf{n}_l, \quad (26)$$

where \mathbf{n}_l are measurement noises. For simplicity, we parameterize the line-broadening function $\boldsymbol{\xi}$ by a Gaussian and adopt the dispersion from the mean value derived by Paper VI. The value of the dispersion is fixed throughout the period of the RM data (see Table 1). Again, we assume that the measurement noises \mathbf{n}_l are Gaussian and uncorrelated along both wavelength and time axes. This results in a Gaussian likelihood probability for \mathbf{y}_l as

$$P_l(\mathbf{y}_l | \Theta) = \prod_{ij} \frac{1}{\sqrt{2\pi}\sigma_{ij}} \exp\left(-\frac{(\mathbf{y}_{l,ij} - \mathbf{f}_{l,ij})^2}{2\sigma_{ij}^2}\right), \quad (27)$$

where Θ denotes the whole set of involved model parameters listed in Table 2, i and j represent the epoch and wavelength bin, and σ_{ij} is the measurement noise.

5.2. Bayesian Inference

The RM data (\mathbf{D}) at hand are the time series of continuum \mathbf{y}_c and emission line \mathbf{y}_l and their respective associated measurement errors. We first use Equation (10) to generate realizations for the continuum time series, which are then used as input for deriving time series of emission line with Equations (17) and (22). In this regard, the continuum data are treated as a prior for BLR modeling (A. Pancoast, private communications; Pancoast et al. 2011, 2014a). From this paradigm, the likelihood probability for \mathbf{D} is thereby

$$P(\mathbf{D} | \Theta) = P(\mathbf{y}_l | \Theta). \quad (28)$$

According to the Bayes’ theorem, the posterior probability distribution for the parameter set Θ is

$$P(\Theta | \mathbf{D}) = \frac{P(\Theta)P(\mathbf{D} | \Theta)}{P(\mathbf{D})}, \quad (29)$$

where $P(\Theta)$ is the prior for the parameter set and $P(\mathbf{D})$ is the Bayesian evidence that just plays the role of normalization factor and important for model selection. The priors for \mathbf{u}_s and \mathbf{u}_q are Gaussian, as described in Section 3. The priors for the other parameters are listed in Table 2, which are assigned following the convention that for parameters whose typical value ranges are known, a uniform prior is assigned; otherwise, if the parameter information is completely unknown, a logarithmic prior is assigned (Sivia & Skilling 2006, Chapter 5). For all the priors, we set a reasonably broad but still finite range to avoid the posterior impropriety.

We include an extra noise parameter $\sigma_{s,l}$, added in square to the measurement noises of emission line data. This is based on two considerations: the present model for BLRs is simple

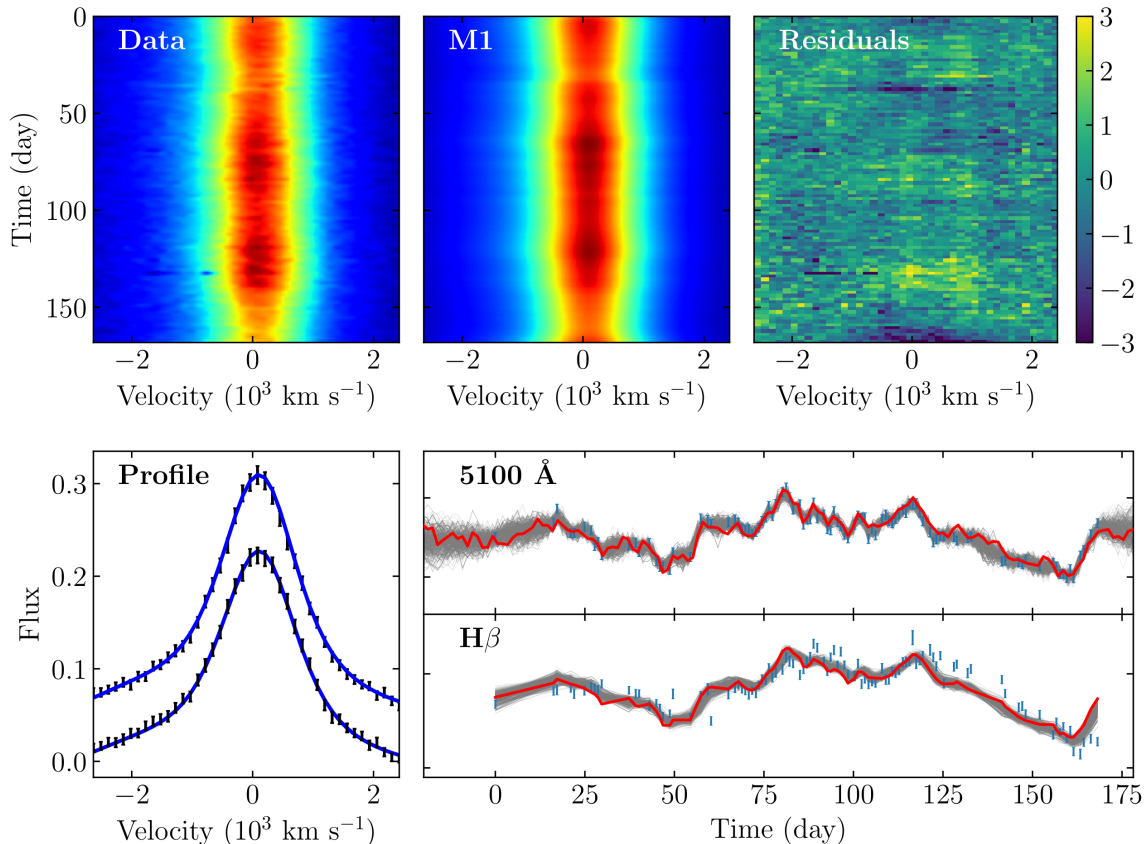


Figure 3. Fits to the RM data of Mrk 142 with BLR model $M1$. Top three panels show the observed $H\beta$ spectral time series, a model fit, and the residuals between the observed data and model fit, which are normalized by the square of the measurement errors. Bottom left panel shows $H\beta$ profiles at two selected epochs, superposed upon the model fits with blue solid lines. Bottom right panels show the time series of the 5100 Å continuum and $H\beta$ fluxes. Red line shows the best recovered time series and light grey lines represent random reconstructions. The observations are set to start at day zero.

so that it unlikely fits all the features of data; on the other hand, there are probably additional noises beyond the known measurement uncertainties. Another additional advantage of using an extra noise parameter is that this provides a very useful annealing operation that benefits the convergences of Markov chains (see below) when the initial parameter values are far from the best-fitting values.

In Table 2, we list the overall free parameters for continuum and BLR modeling. We use 200 points to describe continuum light curve, leading to a total of hundreds of free parameters. Meanwhile, there are strong correlations among BLR parameters, such as inclination and BH mass. This requires sophisticated algorithms that can handle massive and highly correlated parameters. We use the Markov Chain Monte Carlo (MCMC) method to construct samples from the posterior distribution and determine the best-fitting estimate for the parameters. We employ the diffusive nested sampling (DNS) algorithm proposed by Brewer et al. (2011a) to generate the Markov chains. The DNS algorithm is effective at exploring multimodal distributions and strong correlations between parameters. It also allows us to calculate the Bayesian evidence, which can be used for sub-

sequent model selection. Moreover, the DNS algorithm is inherently parallel and is easy to implement on parallel computing interfaces. We write our own DNS code in C language using the standardized Message Passing Interface (MPI) so that the code is portable to a wide range of supercomputer clusters without any reliance on special features of proprietary compilers. We develop a code named BRAINS to implement the above BLR dynamical modeling and Bayesian inference, which is publicly available at <https://github.com/LiyuAstroph/BRAINS>. Unless stated otherwise, throughout the calculations, the best estimates for the parameters are taken to be the median values of their posterior distributions and the uncertainties are determined from the 68.3% confidence intervals.

6. RESULTS

6.1. Overview

Figures 3-5 show the fitting results to the RM data of Mrk 142 with BLR models $M1$, $M2$, and $M3$, respectively. In each figure, the top three panels plot the observed $H\beta$ spectral time series, an exemplary model fit, and the residuals between the data and the fit, respectively. The bottom

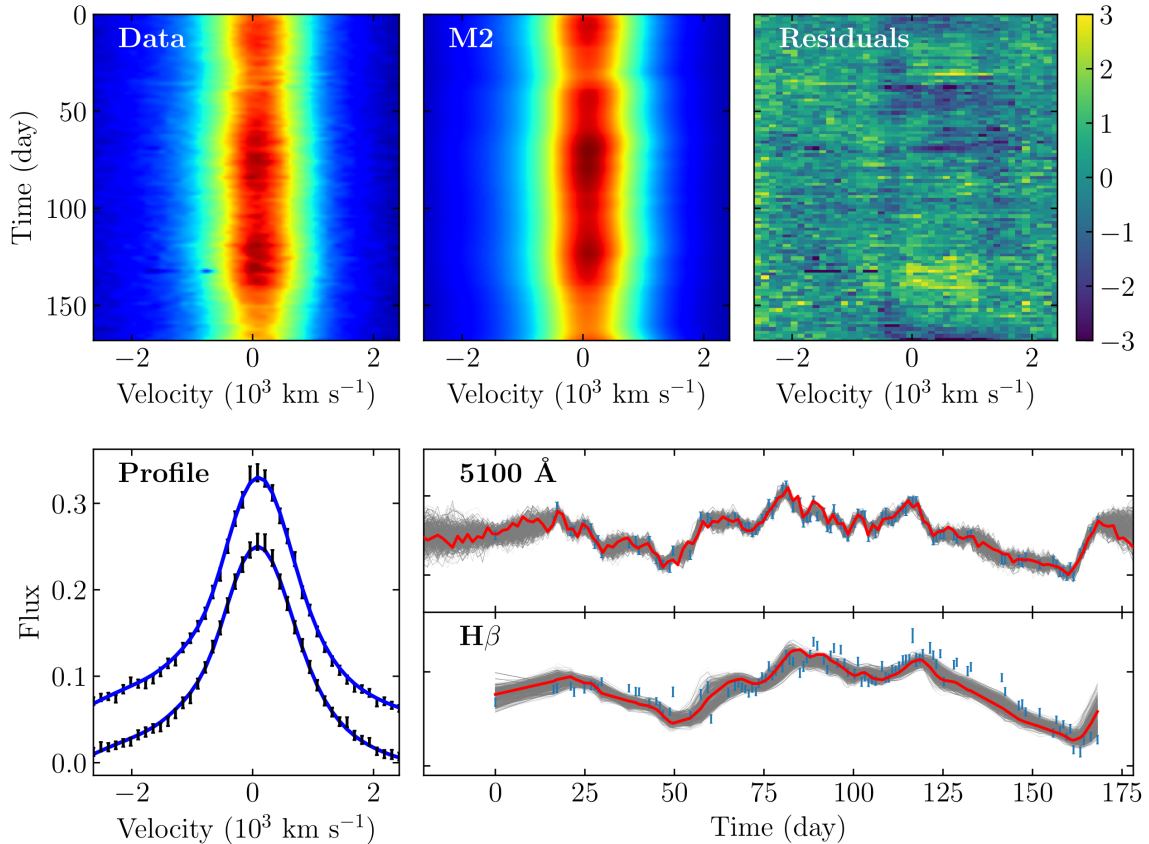


Figure 4. Same as Figure 3 but for BLR model $M2$.

Table 3. Comparison of the three BLR models $M1$, $M2$, and $M3$.

	$M1$	$M2$	$M3$
$\ln \mathcal{L}_{\max}$	0	-280	164
BIC	0	288	-105
AIC	0	562	-313
$\log K$	0	-118	68

NOTE— K is the Bayes factor and all values are given with respect to model $M1$.

panels plot the recovered $H\beta$ profiles at two selected epochs and the reconstructed light curves of the continuum and $H\beta$ fluxes. The three models can generally well reproduce the continuum and $H\beta$ flux light curves, but differ with varying degrees of success in reproducing the detailed $H\beta$ spectral time series. The obtained residuals between the data and model fit illustrate that the fits of $M2$ model have systematic deviations around ~ -500 km s $^{-1}$ and ± 1500 km s $^{-1}$ of $H\beta$ profiles. Models $M1$ and $M3$ give similar fitting to the data, with $M3$ slightly better by visual inspection. Figure 6 shows examples of inferred geometry of the BLR for the three models. In Figure 7, we plot the posterior distributions of BH mass obtained by the three models. The best inferred BH mass is $\log(M_{\bullet}/M_{\odot}) = 5.90^{+0.31}_{-0.31}$, $6.34^{+0.37}_{-0.25}$, and $6.23^{+0.23}_{-0.45}$ for

$M1$, $M2$, and $M3$, respectively. These values are consistent with each other to within uncertainties. The inferred values for the major parameters of the three models are tabulated in Appendix A.

We use the standard approaches of model comparison to determine the best model. In Table 3, we calculate the maximum likelihood ($\ln \mathcal{L}_{\max}$), the Bayesian information criterion (BIC²), the Akaike information criterion (AIC³), and the Bayes factor⁴ for the three models. The best model is chosen to be the one that maximizes the \mathcal{L}_{\max} and Bayes factor and

² The BIC is defined by (Schwarz 1978)

$$\text{BIC} = k \ln n - 2 \ln \mathcal{L}_{\max}, \quad (30)$$

where k is the number of model parameters, n is the sample size, and \mathcal{L}_{\max} is the maximum value of the likelihood function.

³ The AIC is defined by (Akaike 1973)

$$\text{AIC} = 2k - 2 \ln \mathcal{L}_{\max}, \quad (31)$$

where k is the number of model parameters. The original form of AIC is only strictly valid asymptotically. Hurvich Tsai (1989) proposed a correction to AIC for finite sample size, defined as

$$\text{AIC} = 2k - 2 \ln \mathcal{L}_{\max} + \frac{2k(k+1)}{n-k-1}, \quad (32)$$

where n is the sample size. We use this corrected AIC in our calculations.

⁴ Bayes factor is defined by the ratio of the posterior probabilities (Sivia & Skilling 2006). For two models, say $M1$ and $M2$ with equal priors, the

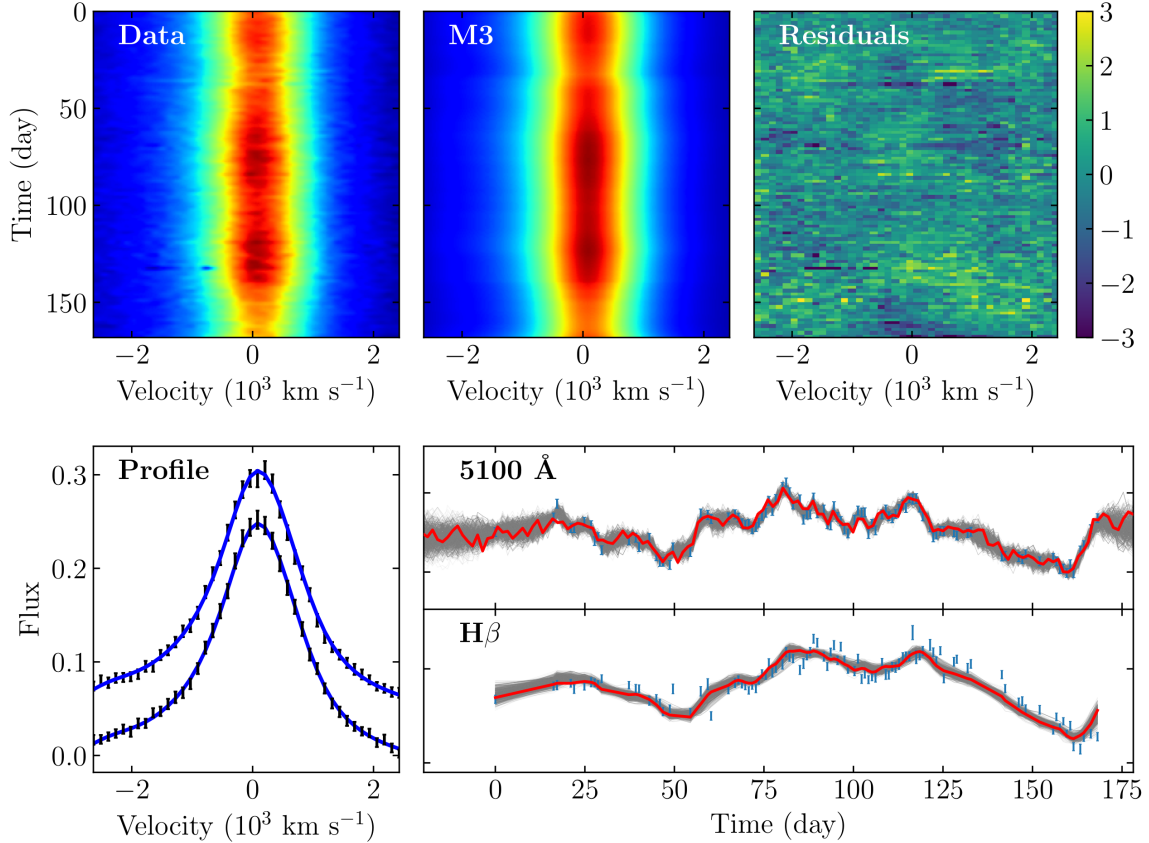


Figure 5. Same as Figure 3 but for BLR model *M3*.

minimizes the AIC and BIC. All the approaches rank model *M3* as the best model for fitting the RM data of Mrk 142. In the following, we study the BLR structure in Mrk 142 based only on the results from model *M3*.

Figure 8 plots the obtained transfer functions and the reconstructed $H\beta$ light curves over selected velocity bins. At each velocity bins, the transfer function peaks at zero lag and then gradually decreases, typical features seen in transfer functions of inclined disk-like BLRs (e.g., Goad & Wanders 1996; Pancoast et al. 2014b). We note that the variability characteristic⁵ at all the velocity bins is generally small ($F_{\text{var}} \sim 7\%$). Compared with AGNs at sub-Eddington accre-

tion rates, low variation amplitudes are a major challenge for monitoring SEAMBH objects (Rakshit & Stalin 2017).

An example of two-dimensional transfer function is shown in the top left panel of Figure 9. It is slightly asymmetric with longer response at red side of the $H\beta$ profile. Such an asymmetric feature is more clearly seen in the velocity-binned delay map in the top right panel. This asymmetry is mainly caused by the anisotropic parameter $\kappa \neq 0$ which means that particles' emissions depend on the locations and also by the dynamical parameter $f_{\text{ellip}} < 1$ which means that particles have inflow ($f_{\text{flow}} < 0.5$) or outflow ($f_{\text{flow}} > 0.5$) motion (see Figure 10). The bottom left panel of Figure 9 plots the delay integral of transfer function $\Psi(v)$, in good agreement with the scaled mean $H\beta$ profile as expected from Equation (25).

6.2. The Structure and Dynamics of the Two-zone BLR

The best model *M3* indicates that the BLR in Mrk 142 consists of two regions, consistent with the self-shadowing effects of slim accretion disk models (Wang et al. 2014b). In Figure 10, we plot the inferred posterior distributions of several selected main parameters in model *M3*. The top panels shows the common parameters for both zones I and II (see the schematic in Figure 2). The bottom panels show the distributions of the parameters for zone I in red and zone II in blue. The inclination angle is 41_{-11}^{+21} . The anisotropic parameter κ peaks at either -0.5 or 0.5 , which means that the observer sees the majority of emissions from either near side

Bayes factor is equal to the ratio of the corresponding Bayesian evidence

$$K = \frac{P(M2|D)}{P(M1|D)} = \frac{P(D|M2)}{P(D|M1)}. \quad (33)$$

⁵ The variability characteristic of a light curve is defined to be (Rodríguez-Pascual et al. 1997)

$$F_{\text{var}} = \frac{(\sigma^2 - \Delta^2)^{1/2}}{\langle F \rangle}, \quad (34)$$

where $\langle F \rangle$ is the averaged flux and

$$\sigma^2 = \frac{1}{N-1} \sum_{i=1}^N (F_i - \langle F \rangle)^2, \quad \Delta^2 = \frac{1}{N} \sum_{i=1}^N \Delta_i^2, \quad (35)$$

where N is the number of points and Δ_i is the uncertainty on the flux F_i .

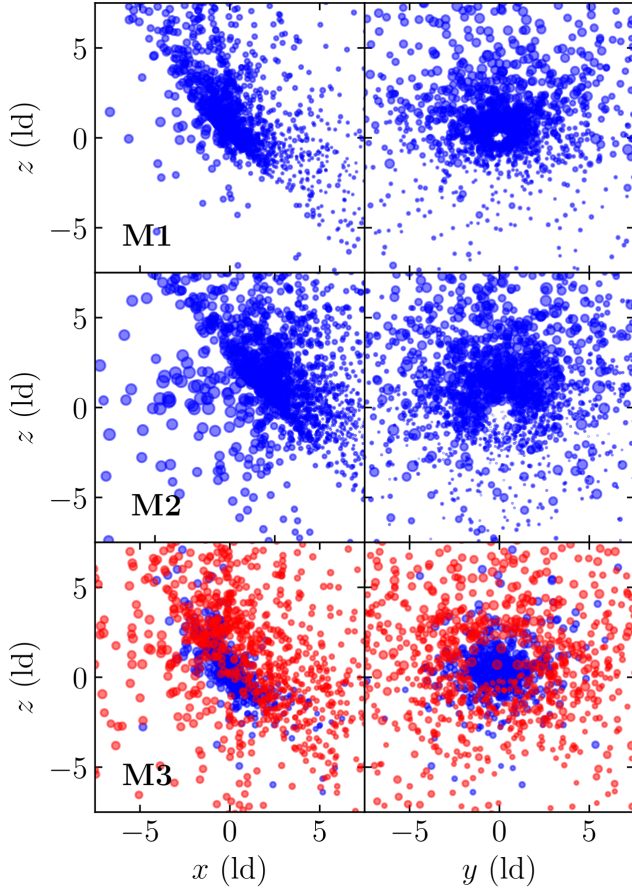


Figure 6. Examples of inferred geometry of the BLR for the three models from top to bottom. Each point represents a BLR particle and its size is in proportional to the weight of emissivity in Equation (15). For model M3, red and blue points correspond to BLR particles from zone I and zone II, respectively.

or far side of the BLR. The parameter γ has a broad distribution over (1, 5), but tends to peak at $\gamma = 5$, indicating that the particles tend to concentrate near the outer face of the BLR disks. The distribution of ξ is also broad and peak around $\xi = 0$, which corresponds to a completely obscured half of the BLR below the equatorial plane.

From the bottom panels of Figure 10, we see that the distributions of the dynamical parameters f_{ellip} and f_{flow} are roughly similar for zones I and II. However, the mean radius μ and the opening angle θ_{opn} are different. Remarkably, the mean radius of zone I is clearly larger than that of zone II, in agreement with the theoretical model proposed by Wang et al. (2014b). Because of the self-shadowing effects of the inner funnel of geometrically thick slim disks, the ionizing continuum flux received by zone II is significantly lower than that received by zone I, leading to a shrunken BLR size of zone II. The ratio of the size scales of the two zones can be

approximated by (Wang et al. 2014b)

$$\frac{\langle R \rangle_{\text{I}}}{\langle R \rangle_{\text{II}}} \approx 2 \times \left(\frac{\dot{M}}{50} \right)^{0.3}. \quad (36)$$

Using the accretion rate $\log \dot{M} = 2.4^{+1.3}_{-0.6}$ for Mrk 142 obtained below, the anticipated ratio is $\log(\langle R \rangle_{\text{I}}/\langle R \rangle_{\text{II}}) = 0.5^{+0.4}_{-0.2}$. Our results give $\log(\langle R \rangle_{\text{I}}/\text{ltid}) = 1.22^{+0.21}_{-0.39}$ and $\log(\langle R \rangle_{\text{II}}/\text{ltid}) = 0.09^{+0.44}_{-0.66}$, marginally consistent with the anticipated value to within uncertainties.

6.3. Comparison with the Cross-Correlation Analysis

In Figure 9, we compare the velocity-binned time lags from our model fitting with these from CCF analysis over velocity bins chosen to be the same as those in Paper VI. We only use the velocity bins with the maximum correlation coefficients $r_{\text{max}} \geq 0.7$. At each velocity bin, the cross-correlation is calculated using the standard interpolated CCF method (Gaskell & Peterson 1987). The time delay is determined by either measuring the location τ_{peak} of the CCF peak (r_{max}) or the centroid τ_{cent} of the points around the peak above the threshold $r \geq 0.8r_{\text{max}}$. As for model fitting, we calculate τ_{peak} and τ_{cent} by cross-correlating the observed continuum light curve with the reconstructed $\text{H}\beta$ light curves interpolated to the observed epochs. There is a tendency that the time lags from model fitting are slightly shorter than these from CCF analysis. We ascribe such a discrepancy to the reason that the CCF (between the observed continuum and $\text{H}\beta$ light curves) are broad and possibly multimodal, as seen from the bottom right panel of Figure 9. Nevertheless, the time lags from two approaches are consistent within uncertainties (at 2σ confidence level). The velocity-binned time lags show an asymmetric pattern with slightly longer lags at red side, which is usually regarded to be a signature of outflowing BLR (see the discussion in Paper VI). Our modeling results in Figure 10 show that the values of the dynamical parameter f_{flow} for both zones I and II distributes over a broad range, meaning that both inflow and outflow can fit the RM data.

6.4. The BH Mass in Mrk 142

Mrk 142 was previously monitored by the LAMP project (Bentz et al. 2009). The obtained $\text{H}\beta$ centroid lag is as short as $2.74^{+0.73}_{-0.83}$ days, in contrast to the anticipated lag of ~ 20 days⁶, making it a significant outlier in the BLR size-luminosity relation (Bentz et al. 2013). The estimated BH mass is $\log(M_{\bullet}/M_{\odot}) = 6.23^{+0.13}_{-0.21}$ using the $\text{H}\beta$ line dispersion of $859 \pm 102 \text{ km s}^{-1}$ from the RMS spectrum and a virial factor of $f_{\text{RMS},\sigma} = 5.5$ (Bentz et al. 2009). In our new observations for Mrk 142, the measured $\text{H}\beta$ centroid lag is $7.9^{+1.2}_{-1.1}$ days through CCF analysis (Paper III) and the estimated BH

⁶ However, Li et al. (2013) reanalyzed the same data (velocity-unresolved) with an approach similar to this work and obtained an $\text{H}\beta$ lag of ~ 15 days, consistent with the anticipated value.

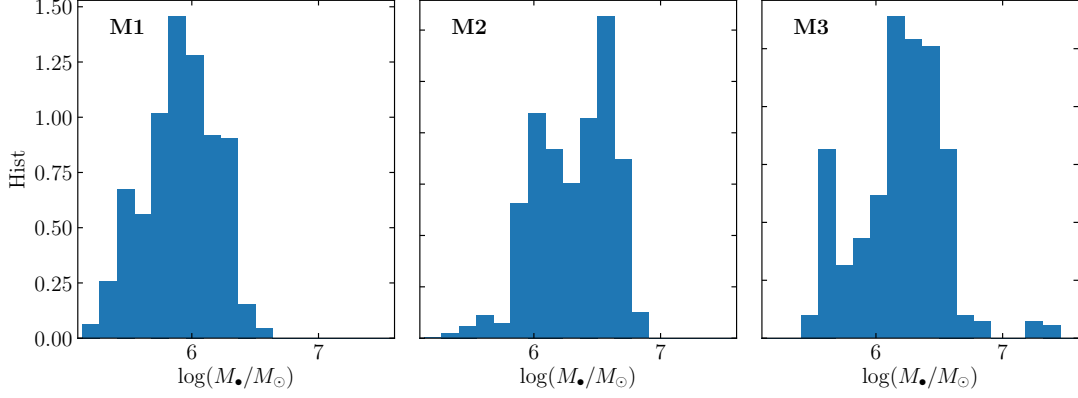


Figure 7. Posterior distributions of BH mass obtained with BLR models *M1*, *M2*, and *M3*.

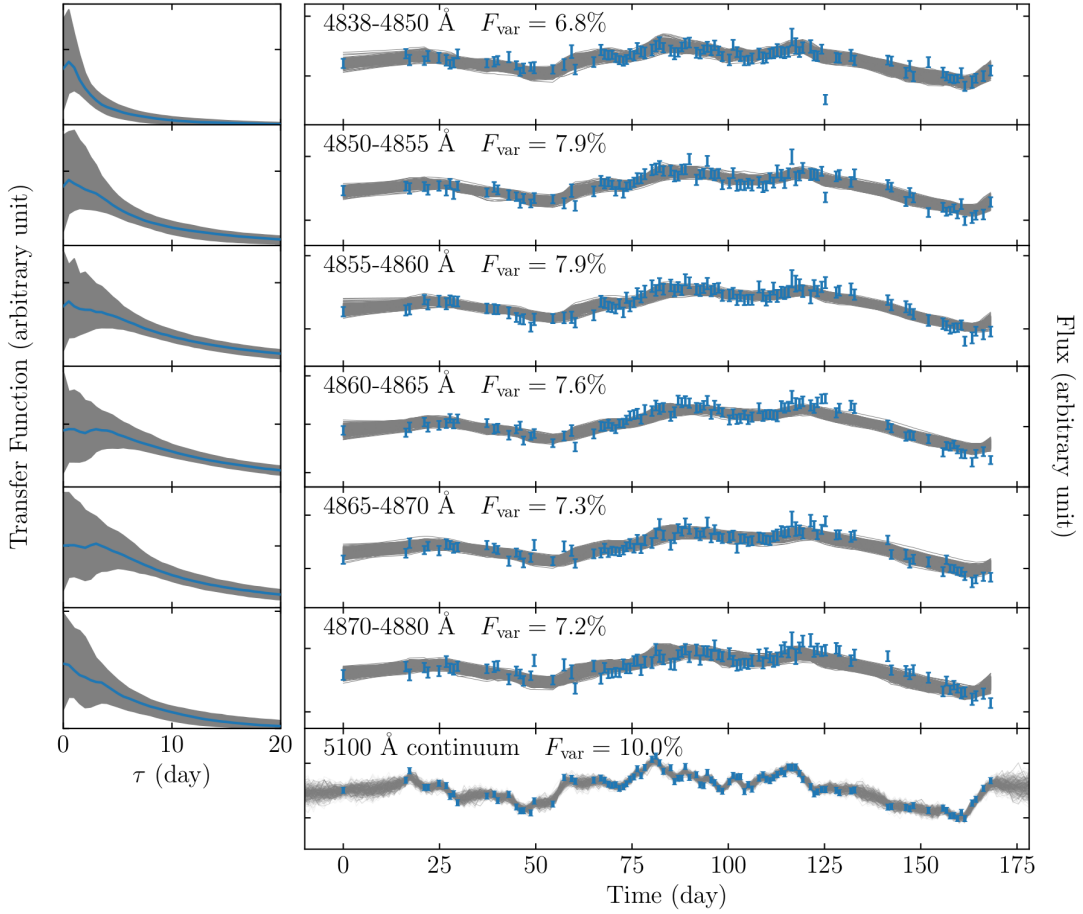


Figure 8. (Left panels) The obtained transfer functions based on model *M3* at selected wavelength bins marked in right panels. Grey shaded areas represent the 1σ error band. (Right panels) The reconstructed light curves. Each thin grey line represents one random reconstruction. Points with errorbars are the observed data. The variability characteristic F_{var} of each observed light curve is also shown.

mass is $\log(M_{\bullet}/M_{\odot}) = 6.59^{+0.07}_{-0.07}$ using the $H\beta$ FWHM from the mean spectrum and a virial factor of $f_{\text{mean,FWHM}} = 1$.

Our model *M3* yields a BH mass of $\log(M_{\bullet}/M_{\odot}) = 6.23^{+0.26}_{-0.45}$ for Mrk 142, in remarkable agreement with [Bentz et al. \(2009\)](#)'s measurement. The resulting virial factor is $\log f_{\text{mean,FWHM}} = -0.36^{+0.33}_{-0.54}$ and $\log f_{\text{RMS,FWHM}} = -0.40^{+0.34}_{-0.56}$

for the $H\beta$ FWHM measured from the mean and RMS spectra, respectively, and $\log f_{\text{mean},\sigma} = 0.07^{+0.31}_{-0.52}$ and $\log f_{\text{RMS},\sigma} = -0.06^{+0.30}_{-0.52}$ for the $H\beta$ line dispersion measured from the mean and RMS spectra, respectively. There have been a number of f calibrations reported in the literature, mainly based on $H\beta$ line dispersion measured from RMS spec-

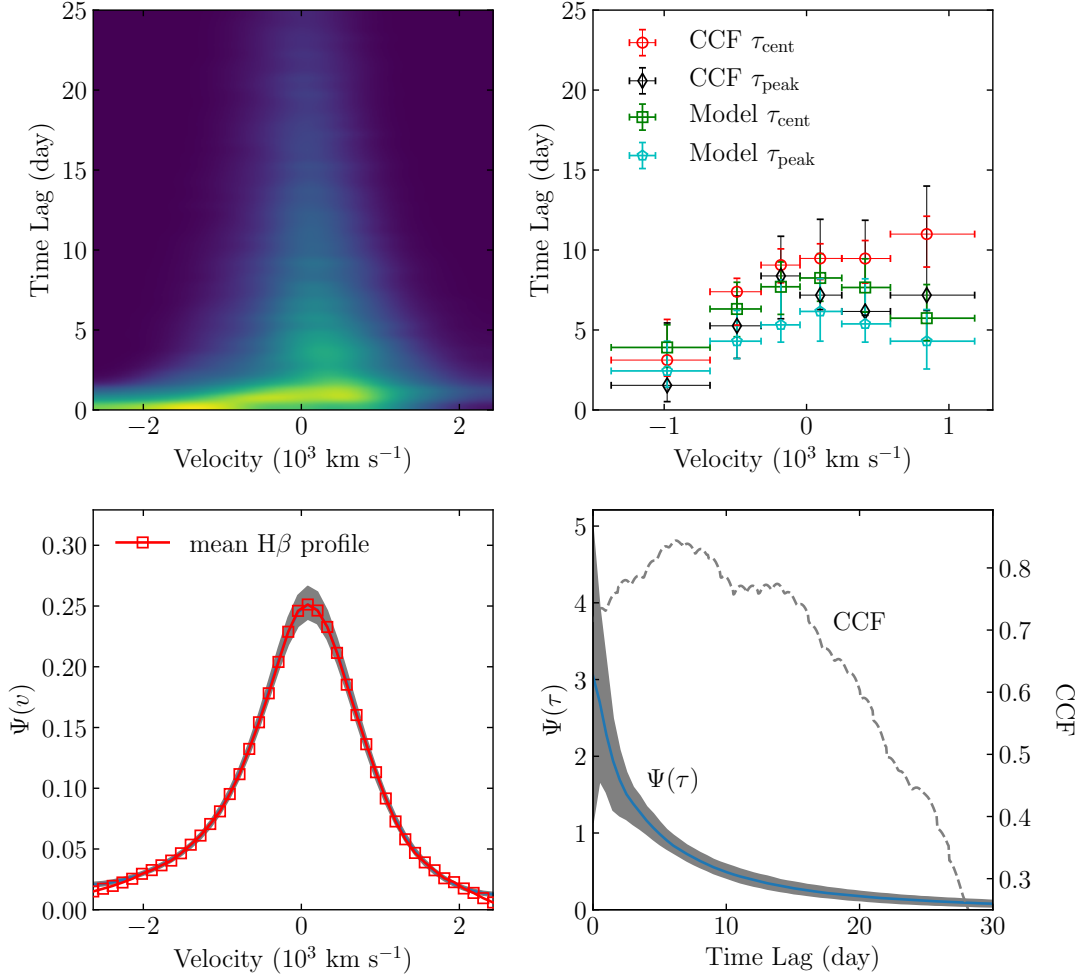


Figure 9. (Top left) An example of transfer function obtained using model *M3*. (Top right) Comparison of velocity-binned time lags obtained from model *M3* and CCF analysis. (Bottom left) Delay integral of transfer function $\Psi(v)$, superposed on the observed, scaled mean $\text{H}\beta$ profile. Shaded areas represent the 1σ error band. (Bottom right) Velocity integral of transfer function $\Psi(\tau)$. Shaded areas represent the 1σ error band. Dashed line represents the CCF between the observed light curves of continuum and $\text{H}\beta$ fluxes.

tra (e.g., Onken et al. 2004; Graham et al. 2011; Park et al. 2012; Woo et al. 2013; Grier et al. 2013a). The calibrated value ranges from $\log f_{\text{RMS},\sigma} = 0.45^{+0.10}_{-0.09}$ (Graham et al. 2011) to $\log f_{\text{RMS},\sigma} = 0.77^{+0.13}_{-0.13}$ (Woo et al. 2013). Ho & Kim (2014) calibrated f factors for AGNs with classical and pseudo bulges separately based on the notion that classical and pseudo bulges obey different $M_{\bullet} - \sigma_{*}$ relations (Kormendy & Ho 2013). They presented f factors for classical and pseudo bulges separately in cases of four widely used measures of $\text{H}\beta$ line widths, namely, FWHM and line dispersion from mean and RMS spectra. Table 4 summarizes the measurements of f factor in the literature. Despite the large uncertainties (~ 0.4 dex), our obtained f factors tend to coincide with the factors for pseudo bulges calibrated by Ho & Kim (2014). The host galaxy of Mrk 142 is a late-type spiral galaxy and shows a strong bar in the nucleus (Ohta et al. 2007). Also, the surface brightness decomposition of the *HST* image does not detect a notable bulge component

(Bentz et al. 2013, Paper I), probably implying that Mrk 142 may not host a classical bulge.

Meanwhile, Pancoast et al. (2014b), Grier et al. (2017), and Williams et al. (2018) applied the BLR dynamical modeling analysis developed by Pancoast et al. (2014a) to a sample of AGNs. By combining the f factor measurements obtained in the three studies, Williams et al. (2018) reported the mean f factors: $\log f_{\text{mean,FWHM}} = 0.00 \pm 0.14$, $\log f_{\text{mean},\sigma} = 0.43 \pm 0.09$, and $\log f_{\text{RMS},\sigma} = 0.57 \pm 0.09$ (see Table 4). Our measured f factors for Mrk 142 are marginally consistent with these results to within uncertainties.

We estimate the dimensionless accretion rate according to the equation (Paper I)

$$\dot{M} = 20.1 \times \left(\frac{L_{5100}}{10^{44} \cos \theta_{\text{inc}}} \right)^{3/2} \left(\frac{M_{\bullet}}{10^7 M_{\odot}} \right)^{-2}. \quad (37)$$

Using the 5100 Å luminosity $\log L_{5100} = 43.56 \pm 0.06$ (Paper IV), the inclination angle $\theta_{\text{inc}} = 41^{+21}_{-11}$ degrees, and the BH

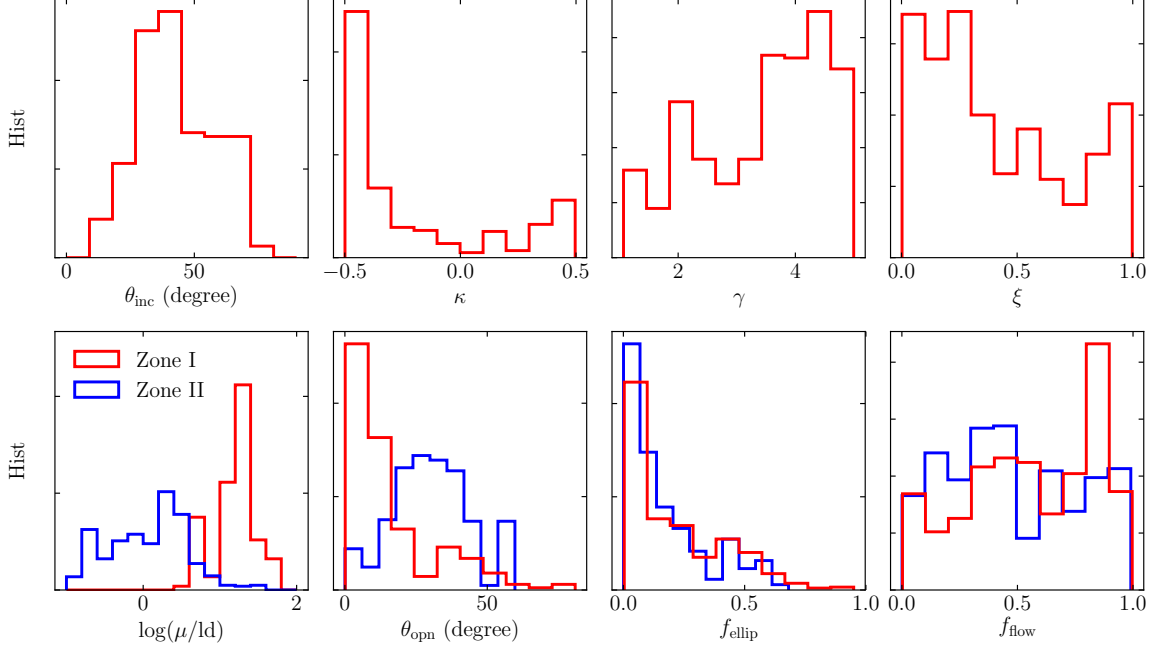


Figure 10. Inferred posterior distributions of the selected main parameters for model *M3*. Top panels are for the common parameters of BLR zones I and II (see the schematic in Figure 2). Bottom panels show the distributions of the parameters for zone I in red and zone II in blue.

Table 4. A summary for f factor measurements.

f factor	Value	Ref	Note
$\log f_{\text{RMS},\sigma}$	$0.74^{+0.12}_{-0.16}$	1	...
	$0.45^{+0.10}_{-0.09}$	2	...
	$0.71^{+0.11}_{-0.11}$	3	...
	$0.77^{+0.13}_{-0.13}$	4	...
	$0.63^{+0.09}_{-0.12}$	5	...
	$0.80^{+0.09}_{-0.12}$	6	classical bulges
	$0.51^{+0.09}_{-0.11}$	6	pseudo bulges
	$0.57^{+0.07}_{-0.07}$	7	dynamical modeling
$\log f_{\text{RMS,FWHM}}$	$-0.06^{+0.30}_{-0.52}$	8	dynamical modeling
	$0.18^{+0.10}_{-0.13}$	6	classical bulges
	$-0.15^{+0.11}_{-0.15}$	6	pseudo bulges
$\log f_{\text{mean},\sigma}$	$-0.40^{+0.34}_{-0.56}$	8	dynamical modeling
	$0.75^{+0.09}_{-0.11}$	6	classical bulges
	$0.28^{+0.14}_{-0.20}$	6	pseudo bulges
	$0.43^{+0.09}_{-0.09}$	7	dynamical modeling
$\log f_{\text{mean,FWHM}}$	$0.07^{+0.31}_{-0.52}$	8	dynamical modeling
	$0.11^{+0.12}_{-0.16}$	6	classical bulges
	$-0.30^{+0.15}_{-0.22}$	6	pseudo bulges
	$0.00^{+0.14}_{-0.14}$	7	dynamical modeling
	$-0.36^{+0.33}_{-0.54}$	8	dynamical modeling

References—(1) Onken et al. (2004), (2) Graham et al. (2011), (3) Park et al. (2012), (4) Woo et al. (2013), (5) Grier et al. (2013a), (6) Ho & Kim (2014), (7) Williams et al. (2018), and (8) this work.

mass $\log(M_{\bullet}/M_{\odot}) = 6.23^{+0.23}_{-0.45}$, we obtain $\log \dot{M} = 2.4^{+1.3}_{-0.6}$. This confirms the BH in Mrk 142 to be an SEAMBH accreting at a super-Eddington rate.

7. DISCUSSIONS

7.1. The Continuum Reconstruction by the DRW Process

The continuum light curve is reconstructed using the DRW process, which is found to be sufficiently adequate for large samples of AGN light curves on timescales of weeks to years (e.g., Kelly et al. 2009; MacLeod et al. 2010; Zu et al. 2011, 2013; Andrae et al. 2013; Kozłowski 2016a). However, on short timescales of days, there is evidence for deviations from DRW process for high-cadence AGN light curves monitored by the *Kepler* telescope (Mushotzky et al. 2011; Kasliwal et al. 2015; Kozłowski 2016b). Kelly et al. (2014) proposed to use the generic continuous-time autoregressive moving average (CARMA) models to characterize the variability features of a broad range of stochastic light curves. The DRW process is a special case of CARMA processes with autoregressive order $p = 0$ and moving average order $q = 0$. Using the package `CARMAPACK`⁷ developed by Kelly et al. (2014), we can choose the best order of p and q for CARMA processes by minimizing the AIC. We find that DRW process is still the favorable model compared with high-order of CARMA processes for the data of Mrk 142. In addition, using the Bayesian framework proposed by Li & Wang (2018), we perform comparison between the DRW model and the power spectral density (PSD) model with a single power-law. Note that the DRW model has a $\text{PSD} \propto 1/[1+(f/f_0)^2]$, where f is the frequency and $f_0 = 1/2\pi\tau_d$. We confirm that the DRW model is slightly preferable.

⁷ Accessible at https://github.com/brandonckelly/carma_pack.

On the other hand, different continuum models mainly affect the short time-scale variability of the reconstructed continuum between measurement points (e.g., see Li & Wang 2018). Such an effect will finally influence the amplitudes of the inferred parameter uncertainties. However, the inherent convolution operation in RM analysis (see Equation 19) will largely smooth the short time-scale variations. We therefore expect that the estimated uncertainties should not be significantly affected by the details of the chosen continuum models (see also discussions in Skielboe et al. 2015 and Fausnaugh et al. 2018).

7.2. Anisotropic Emission of the Central Ionizing Source

We only take into account the possibility that the anisotropic ionizing emission from the geometrically thick funnel in the inner region of slim accretion disks produce two-zone BLRs. Indeed, there are two additional anisotropic effects for accretion disks. First, the ionizing emissions strongly depend on the angle between the symmetric axis of disks and the direction toward BLR particles. Second, the sizes of the ionizing source may be no longer negligible when in particular using 5100 Å continuum as a surrogate for ionizing continuum (see also Section 7.3). The first effect will cause the BLR to be thicker to compensate the $\cos\theta$ dependence of the disk emission. To include the second effect, one needs to solve the structure of accretion disks and obtain the radial distribution of emissions. This will make the present model more complicated and the MCMC sampling more inefficient. We are thus content with the present simple treatments on the ionizing sources and defer the inclusion of these two effects to a separate paper.

7.3. Point-like Geometry of the Central Ionizing Source

We implicitly assume that the emission region of the 5100 Å continuum is point-like. However, multiwavelength RM observations on a handful of AGNs indeed detected time lags of the optical continuum variations with respect to the X-ray/UV variations (e.g., Edelson et al. 2015, 2017; Cackett et al. 2018; Fausnaugh et al. 2018). This indicates that the emission region at 5100 Å could be spatially extended. We can estimate the characteristic radius for emission of the 5100 Å continuum using the standard accretion disk model. The local effective temperature of the accretion disk is written (e.g., Laor & Davis 2011)

$$T(r) = f(r, a) \left(\frac{3c^6}{8\pi G^2 \sigma} \right)^{1/4} \frac{\dot{M}^{1/4}}{M_\bullet^{1/2}} r^{-3/4}, \quad (38)$$

where $r = R/R_g$, R_g is the gravitational radius, a is the BH spin, $\dot{M} = \mathcal{M} L_{\text{Edd}}/c^2$ is the mass accretion rate, M_\bullet is the BH mass, σ is the Stefan-Boltzmann constant, and $f(r, a)$ is a dimensionless factor on the order of unity that is set by the inner boundary condition and the relativistic effects. Regardless of $f(r, a)$ and using $\log \mathcal{M} = 2.4^{+1.3}_{-0.6}$ and $\log(M_\bullet/M_\odot) = 6.23^{+0.23}_{-0.45}$, the corresponding radius for the 5100 Å emission is $R_{5100} = 0.14^{+0.60}_{-0.11}$ ld. Note that for a slim disk, the presence of

prominent radial advection reduces the effective temperature (Abramowicz et al. 1988; Wang & Zhou 1999), making the above estimate conservative. Considering that the inferred disk size from multiwavelength reverberation mapping observations is about 3 times larger than that predicted from the standard disk model (e.g., Edelson et al. 2015), the 5100 Å emission radius R_{5100} would be comparable with the mean radius of zone I, but much smaller than the mean radius of zone II (see Table 5). Spatial extension of the 5100 Å emission region may lead the obtained BH mass to be underestimated. It is worth a detailed study for the influences of spatially extended 5100 Å emission region on BH mass measurement. As discussed in the preceding section, for the sake of simplicity, we keep the assumption of point-like geometry of the 5100 Å emission region and defer the detailed study to a future paper.

7.4. Model Dependence of the Results

In the present BLR models, the prescriptions for BLR properties are purely phenomenological and adopted only for the sake of simplicity. This raises an issue as to whether the inferred results depend on the adopted model. To address this issue, we need: 1) independent measurements from alternative approaches, and 2) model selections to evaluate the most probable model for BLRs. A major challenge for performing model selections is that the existing BLR models (see the summary in Table 1 of Wang et al. 2012) invoke complicated physical processes, impeding an efficient MCMC inference. The results from the three BLR models indeed imply that the obtained BH masses appear to be slightly different, although they reproduce the RM data with different degrees of success. Recently, Czerny et al. (2017) developed a self-consistent BLR model based on the failed radiatively accelerated dusty outflow model (Czerny & Hryniewicz 2011), which only invokes the basic physical parameters, such as BH mass and spin, and accretion rate. The model is purely analytic and therefore apt for MCMC realization. A comparison of the inferred parameters from this model and the present dynamical modeling will shed light into the issue as to model dependence of the results.

7.5. Parameter Degeneracy

The significant degeneracy in present models is among the BH mass, the inclination angle and the opening angle. There are two reasons causing this degeneracy (Grier et al. 2017). The first reason is from the model itself, such as the strong correlation between BH mass and inclination angle or opening angle, ascribed to the adopted disk-like geometry for the BLR (Collin et al. 2006; Li et al. 2013). The other reason is from the constraints by observation data. Similar to Pancoast et al. (2014b) and Grier et al. (2017), we also find a tight correlation between inclination and opening angles. Moreover, the values of these two angles are approximately equal. As pointed out by Grier et al. (2017), the interpretations for such behavior are two-fold: first, to generate single-peaked line profiles, the opening angle should be larger than the inclination angle; secondly, as the opening angle increases, the

generated profiles tend to be flat in the core (e.g., [Netzer & Marziani 2010](#)), apparently incompatible with the observed line shapes. Therefore, the observations require the opening angle as small as possible while still large enough to produce single-peaked line profiles. As a result, the opening angle approximately equals to the inclination angle.

7.6. BLR Dynamical Modeling

The present dynamical model does not include possible systematic errors for the model assumptions. This issue can be overcome by comparing mass measurements against these from the other independent techniques, such as stellar dynamics and gas dynamics widely used in quiescent galaxies. Unfortunately, the objects with both RM monitoring and the other independent measurements are still extremely few ([Peterson 2014](#)). On the other hand, new techniques such as spectro-astrometry ([Gnerucci et al. 2010](#); [Stern et al. 2015](#)) and spectro-interferometry ([Kraus 2012](#); [Petrov et al. 2012](#)) are in the process of development with the purpose of spatially resolving gas dynamics surrounding the central BHs using the current ground-based 10m class telescopes ([Gnerucci et al. 2011, 2013](#); [Rakshit et al. 2015](#)). Hopefully, in the near future, there will be sufficient data sample with independent mass measurements that allow us to explore the systematic errors of our dynamical models.

7.7. Comparison with the Maximum Entropy Method

The maximum entropy method (MEM, [Horne 1994](#)) is also widely used to derive transfer functions of BLRs and probe structure and dynamics of BLRs. [Paper VII](#) presented the transfer function for Mrk 142 by applying MEM to the same RM data used in this paper. The obtained transfer function exhibits a major response around 5-10 days (see Figure 11 in [Paper VII](#)), seemingly distinct from the transfer function derived from our dynamical modeling analysis (see the top right panel of Figure 9). However, this is not the case because of the following reasons. First, MEM solves a *modified* equation compared to Equation (19) (regardless of the no-linear response)

$$f_i(v, t) = \bar{f}_i(v) + \int \Psi_{\text{MEM}}(v, \tau) [f_c(t - \tau) - \bar{f}_c] d\tau, \quad (39)$$

where $\bar{f}_i(v)$ and \bar{f}_c are considered to be the constant background terms ([Horne 1994](#)). MEM employs maximum entropy regularization to find the smoothest solutions $\Psi_{\text{MEM}}(v, \tau)$, $\bar{f}_i(v)$, and \bar{f}_c that best fit the observed data. In real implementation, the derived $\bar{f}_i(v)$ and \bar{f}_c usually include contributions from the nonvariable part of the broad emission line and continuum, which cannot be attributed to background contributions ([Wanders 1995](#)). As a result, Ψ_{MEM} is sensitive to changes in the responses of the BLR but insensitive to the total responses of the BLR. In this sense, it is more appropriate to call Ψ_{MEM} “marginal transfer function”.

Second, MEM uses a free parameter to control the trade-off between smoothness of the solutions and goodness of fitting to the data. In practice, the value of this free parameter

is chosen by eye to achieve the best compromise. Sharp features in transfer functions will generally be smeared out by MEM (see also discussions in [Pancoast et al. 2018](#)), so it is not straightforward to perform a direct, quantitative comparison with the results from dynamical modeling.

8. CONCLUSIONS

We employ the recently developed dynamical modeling for broad-line regions to analyze the RM data of broad H β line and 5100 Å continuum for Mrk 142 monitored between 2012 and 2013. The BH mass is self-consistently measured without resort to the virial factor required in the traditional RM analysis through the cross-correlation method. The main results are as follows:

1. We apply three BLR models to fit the RM data of Mrk 142 and find that the best model is a two-zone model (see the schematic in Figure 2), consistent with the theoretical BLR model proposed by [Wang et al. \(2014b\)](#). The two zones may be caused by the anisotropic ionizing emission due to the self-shadowing of the slim accretion disk. Interestingly, the obtained mean size of zone I is larger than that of zone II, also in agreement with the theoretical model. It is possible that a much more complicated one-zone BLR model can also fit the data of Mrk 142. Still, our results are illustrative and application to other SEAMBH objects is required to reinforce the scenario of the two-zone BLR model.
2. The general geometry of H β BLRs for Mrk 142 is described by an inclined disk with an inclination angle of 42_{-11}^{+21} degrees. The opening angles for zones I and II are 30_{-12}^{+14} degrees and 10_{-5}^{+26} degrees, respectively, corresponding to a thick disk with a total height aspect of $h/r \sim 0.6$.
3. The obtained BH mass is $\log(M_{\bullet}/M_{\odot}) = 6.23_{-0.45}^{+0.26}$, resulting in a virial factor of $\log f_{\text{mean,FWHM}} = -0.36_{-0.54}^{+0.33}$ and $\log f_{\text{RMS,FWHM}} = -0.40_{-0.56}^{+0.34}$ for the H β FWHM measured from the mean and RMS spectra, respectively, and $\log f_{\text{mean},\sigma} = 0.07_{-0.52}^{+0.31}$ and $\log f_{\text{RMS},\sigma} = -0.06_{-0.52}^{+0.30}$ for the H β line dispersion measured from the mean and RMS spectra, respectively. These values are consistent to within uncertainties with previous measurements by similarly applying dynamical modeling to a dozen of AGNs ([Pancoast et al. 2014b](#); [Grier et al. 2017](#); [Williams et al. 2018](#)). Our obtained factors appear to coincide with the calibrations by [Ho & Kim \(2014\)](#) using the $M_{\bullet} - \sigma_{\star}$ relation for pseudo bulges. If taking into account the intrinsic scatter (~ 0.3 dex) of the $M_{\bullet} - \sigma_{\star}$ relation ([Kormendy & Ho 2013](#)), our obtained factors are also marginally consistent with other calibrations that did not explicitly make a distinction between morphology of host bulges (e.g., [Onken et al. 2004](#); [Park et al. 2012](#); [Woo et al. 2013](#); [Grier et al. 2013a](#); see Table 4). The resulting dimensionless accretion rate is $\log \dot{M} = 2.4_{-0.6}^{+2.3}$, confirming that the

BH in Mrk 142 is an SEAMBH accreting at super-Eddington rate.

We end by remarking that the present dynamical modeling for BLRs is still at an early stage of infancy. Nevertheless, our application to Mrk 142 along with previous applications to a dozen of AGNs (Pancoast et al. 2012; Brewer et al. 2011b; Pancoast et al. 2014b; Grier et al. 2017; Williams et al. 2018) is enlightening. Compared with the traditional CCF approach, direct modeling of the BLR structure and dynamics can reveal much more information in the RM data and most importantly offers an approach for BH mass measurements without the need of invoking the virial factor. Future improvements of the dynamical modeling should address the issue of the associated systematic errors and incorporate physical processes (such as photoionization and radiation pressure).

We thank the referee for useful suggestions that improve the manuscript. We acknowledge the support of the staff of the Lijiang 2.4 m telescope. Y.R.L. thanks Anna Pancoast and Brendon Brewer for useful discussions on BLR dynam-

ical modeling. This research is supported in part by the National Key R&D Program of China (2016YFA0400700), by the CAS Key Research Program (KJZDEW-M06), and by grant No. NSFC-1113006, and -U1431228 from the National Natural Science Foundation of China. Y.R.L. acknowledges financial support from the National Natural Science Foundation of China through grant No. 11570326 and from the Strategic Priority Research Program of the Chinese Academy of Sciences grant No. XDB23000000. L.K.X. acknowledges financial support from the Light of West China Program (Y7XB016001) and from the National Natural Science Foundation of China through grant No. 11703077. L.C.H. acknowledges financial support from Peking University, the Kavli Foundation, and from the National Natural Science Foundation of China through grant No. 11473002 and also No. 11721303. B.W.H. acknowledges financial support from the National Key R&D Program of China (2017YFA0402703). All the calculations in this work used the computing clusters at the Computer Center of the Institute of High Energy Physics.

Software: BRAINS <https://github.com/LiyAstroph/BRAINS>

APPENDIX

A. INFERRED PARAMETER VALUES FOR THE THREE BLR MODELS

In Table 5, we summarize the inferred values of the major parameters for all three models. The best estimates are taken to be the median values of the posterior distributions and the uncertainties are taken from the 68.3% confidence intervals.

B. A VALIDITY TEST OF THE CODE BRAINS

To test the validity of our code, we generate mock data with the same cadence and spectral resolution as the RM data of Mrk 142 using model *M3* (the two-zone BLR model). Figure 11 shows the fitting results, and Figure 12 shows comparison between the posterior distributions of major parameters of *M3* and the input values. As can be seen, the posterior distributions are generally consistent with the input values.

REFERENCES

- Abramowicz, M. A., Czerny, B., Lasota, J. P., & Szuszkiewicz, E. 1988, *ApJ*, 332, 646
- Akaike, H. 1973, in *Proceedings of the Second International Symposium on Information Theory*, ed. B. Petrov & F. Csaki (Budapest: Akademiai Kiado), 267
- Aoki, K., Kawaguchi, T., & Ohta, K. 2005, *ApJ*, 618, 601
- Andrae, R., Kim, D.-W., & Bailer-Jones, C. A. L. 2013, *A&A*, 554, A137
- Barth, A. J., Bennert, V. N., Canalizo, G., et al. 2015, *ApJS*, 217, 26
- Bentz, M. C., Denney, K. D., Grier, C. J., et al. 2013, *ApJ*, 767, 149
- Bentz, M. C., Walsh, J. L., Barth, A. J., et al. 2009, *ApJ*, 705, 199
- Bentz, M. C., Walsh, J. L., Barth, A. J., et al. 2010, *ApJ*, 716, 993
- Boroson, T. A. 2002, *ApJ*, 565, 78
- Boroson, T. A., & Green, R. F. 1992, *ApJS*, 80, 109
- Brewer, B. J., Páatay, L. B., & Csányi, G. 2011a, *Stat. Comput.*, 21, 649
- Brewer, B. J., Treu, T., Pancoast, A., et al. 2011b, *ApJL*, 733, L33
- Blandford, R. D., & McKee, C. F. 1982, *ApJ*, 255, 419
- Bottorff, M., Korista, K. T., Shlosman, I., & Blandford, R. D. 1997, *ApJ*, 479, 200
- Burbidge, E. M. 1967, *ARA&A*, 5, 399
- Cackett, E. M., Chiang, C.-Y., McHardy, I., et al. 2018, *ApJ*, 857, 53
- Collin, S., Kawaguchi, T., Peterson, B. M., & Vestergaard, M. 2006, *A&A*, 456, 75
- Condon, J. J., Hutchings, J. B., & Gower, A. C. 1985, *AJ*, 90, 1642
- Cromwell, R., & Weymann, R. 1970, *ApJL*, 159,
- Czerny, B., & Hryniewicz, K. 2011, *A&A*, 525, L8
- Czerny, B., Li, Y.-R., Sredzinska, J., et al. 2017, *ApJ*, 846, 154
- Denney, K. D., Peterson, B. M., Pogge, R. W., et al. 2010, *ApJ*, 721, 715
- Du, P., Hu, C., Lu, K.-X., et al. 2014, *ApJ*, 782, 45 (Paper I)
- Du, P., Hu, C., Lu, K.-X., et al. 2015, *ApJ*, 806, 22 (Paper IV)
- Du, P., Lu, K.-X., Zhang, Z.-X., et al. 2016a, *ApJ*, 825, 126 (Paper V)
- Du, P., Lu, K.-X., Hu, C., et al. 2016b, *ApJ*, 820, 27 (Paper VI)
- Du, P., Zhang, Z.-X., Wang, K., et al. 2018, *ApJ*, 856, 6 (Paper IV)

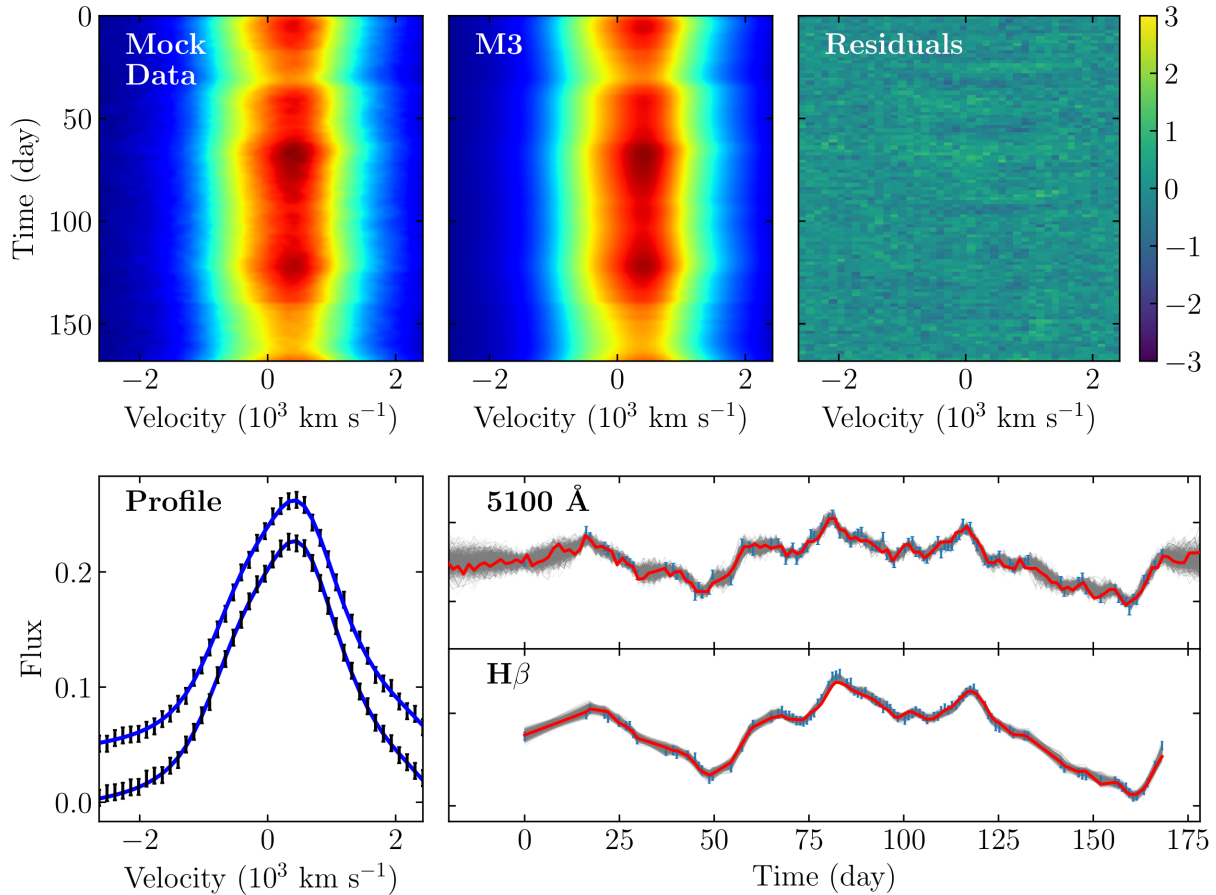


Figure 11. The same as Figure 3, but for fits to mock data generated using BLR model *M3*.

- Edelson, R., Gelbord, J., Cackett, E., et al. 2017, *ApJ*, 840, 41
Edelson, R., Gelbord, J. M., Horne, K., et al. 2015, *ApJ*, 806, 129
Emmering, R. T., Blandford, R. D., & Shlosman, I. 1992, *ApJ*, 385, 460
Fabian, A. C., Rees, M. J., Stella, L., & White, N. E. 1989, *MNRAS*, 238, 729
Fausnaugh, M. M., Starkey, D. A., Horne, K., et al. 2018, *ApJ*, 854, 107
Ferrarese, L., & Merritt, D. 2000, *ApJL*, 539, L9
Gaskell, C. M., & Peterson, B. M. 1987, *ApJS*, 65, 1
Gaskell, C. M., & Sparke, L. S. 1986, *ApJ*, 305, 175
Gebhardt, K., Bender, R., Bower, G., et al. 2000, *ApJL*, 539, L13
Gnerucci, A., Marconi, A., Capetti, A., et al. 2011, *A&A*, 536, 86
Gnerucci, A., Marconi, A., Capetti, A., Axon, D. J., & Robinson, A. 2010, *A&A*, 511, 19
Gnerucci, A., Marconi, A., Capetti, A., Axon, D. J., & Robinson, A. 2013, *A&A*, 549, 139
Goad, M. R., & Korista, K. T. 2014, *MNRAS*, 444, 43
Goad M., Wanders I., 1996, *ApJ*, 469, 113
Graham, A. W., Onken, C. A., Athanassoula, E., & Combes, F. 2011, *MNRAS*, 412, 2211
Greene, J. E., & Ho, L. C. 2007, *ApJ*, 667, 131
Gregory, P. 2005, *Bayesian Logical Data Analysis for the Physical Sciences* (Cambridge: Cambridge Univ. Press)
Gregory, P. C. 2011, *MNRAS*, 410, 94
Grier, C. J., Martini, P., Watson, L. C., et al. 2013a, *ApJ*, 773, 90
Grier, C. J., Pancoast, A., Barth, A. J., et al. 2017, *ApJ*, 849, 146
Grier, C. J., Peterson, B. M., Horne, K., et al. 2013b, *ApJ*, 764, 47
Grier, C. J., Peterson, B. M., Pogge, R. W., et al. 2012, *ApJL*, 744, LL4
Ho, L. 1999, in *Observational Evidence for the Black Holes in the Universe*, ed. S. K. Chakrabarti (Dordrecht: Kluwer), 157
Ho, L. C., & Kim, M. 2014, *ApJ*, 789, 17
Horne, K. 1994, *Reverberation Mapping of the Broad-Line Region in Active Galactic Nuclei*, 69, 23
Hu, C., Du, P., Lu, K.-X., et al. 2015, *ApJ*, 804, 138 (Paper III)
Hu, C., Wang, J.-M., Ho, L. C., et al. 2016, *ApJ*, 832, 197
Hurvich, C. M., & Tsai, C.-L. 1989, *Biometrika*, 76, 297
Kasliwal, V. P., Vogeley, M. S., & Richards, G. T. 2015, *MNRAS*, 451, 4328
Kashi, A., Proga, D., Nagamine, K., Greene, J., & Barth, A. J. 2013, *ApJ*, 778, 50
Kaspi, S., Maoz, D., Netzer, H., et al. 2005, *ApJ*, 629, 61
Kaspi, S., Smith, P. S., Netzer, H., et al. 2000, *ApJ*, 533, 631
Kaspeba, T. M., Peterson, B. M., Wanders, I., et al. 1997, *ApJ*, 475, 106
Kelly, B. C., Bechtold, J., & Siemiginowska, A. 2009, *ApJ*, 698, 895
Kelly, B. C., Becker, A. C., Sobolewska, M., Siemiginowska, A., & Uttley, P. 2014, *ApJ*, 788, 33

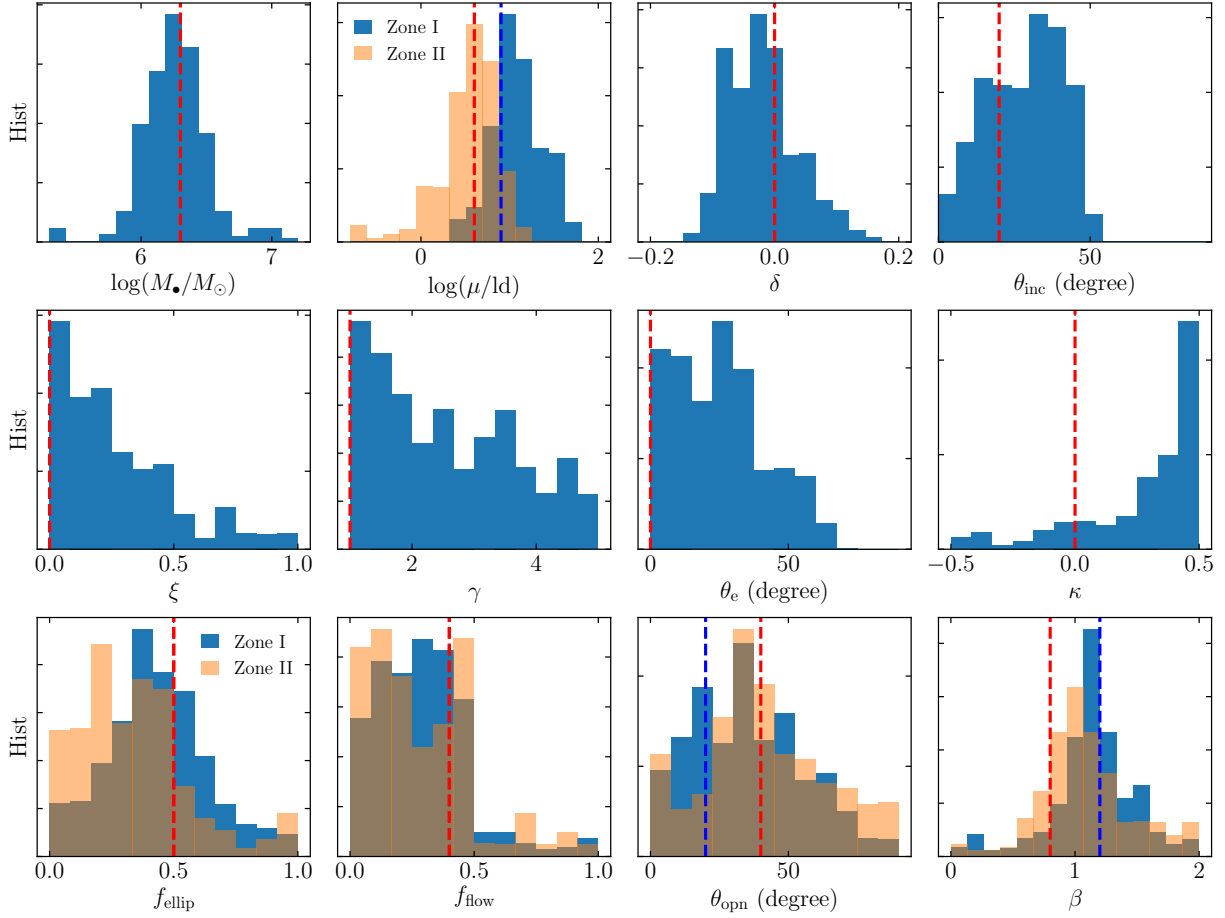


Figure 12. Posterior distributions of the major parameters of model *M3* inferred from the mock data shown in Figure 11. Vertical dashed lines represent the input values for zone I (in blue) AMD zone II (in red). For the common parameters of zones I and II, red dashed line represent the input values. The parameters f_{ellip} and f_{flow} for zones I and II have the same input values.

Koratkar, A. P., & Gaskell, C. M. 1991, *ApJS*, 75, 719
 Kormendy, J., & Bender, R. 2011, *Nature*, 469, 377
 Kormendy, J., Bender, R., & Cornell, M. E. 2011, *Nature*, 469, 374
 Kormendy, J., & Ho, L. C. 2013, *ARA&A*, 51, 511
 Kormendy, J., & Richstone, D. 1995, *ARA&A*, 33, 581
 Kozłowski, S. 2016a, *ApJ*, 826, 118
 Kozłowski, S. 2016b, *MNRAS*, 459, 2787
 Kraus, S. 2012, *Proc. SPIE*, 8445, 84451H
 Krolik, J. H. 2001, *ApJ*, 551, 72
 Laor, A., & Davis, S. W. 2011, *MNRAS*, 417, 681
 Li, Y.-R., & Wang, J.-M. 2018, *MNRAS*, 476, L55
 Li, Y.-R., Wang, J.-M., & Bai, J.-M. 2016, *ApJ*, 831, 206
 Li, Y.-R., Wang, J.-M., Ho, L. C., Du, P., & Bai, J.-M. 2013, *ApJ*, 779, 110
 MacLeod, C. L., Ivezić, Ž., Kochanek, C. S., et al. 2010, *ApJ*, 721, 1014
 Magorrian, J., Tremaine, S., Richstone, D., et al. 1998, *AJ*, 115, 2285
 Maoz, D., Netzer, H., Mazeh, T., et al. 1991, *ApJ*, 367, 493
 Mushotzky, R. F., Edelson, R., Baumgartner, W., & Gandhi, P. 2011, *ApJL*, 743, L12

Netzer, H. 1990, in *Active Galactic Nuclei*, ed. R. D. Blandford, H. Netzer, L. Woltjer, T. J.-L. Courvoisier, & M. Mayor (Berlin: Springer), 57
 Netzer, H. 2009, *ApJ*, 695, 793
 Netzer, H., & Marziani, P. 2010, *ApJ*, 724, 318
 Ohta, K., Aoki, K., Kawaguchi, T., & Kiuchi, G. 2007, *ApJS*, 169, 1
 Onken, C. A., Ferrarese, L., Merritt, D., et al. 2004, *ApJ*, 615, 645
 Pancoast, A., Barth, A. J., Horne, K., et al. 2018, *ApJ*, 856, 108
 Pancoast, A., Brewer, B. J., & Treu, T. 2011, *ApJ*, 730, 139
 Pancoast, A., Brewer, B. J., Treu, T., et al. 2012, *ApJ*, 754, 49
 Pancoast, A., Brewer, B. J., & Treu, T. 2014a, *MNRAS*, 445, 3055
 Pancoast, A., Brewer, B. J., Treu, T., et al. 2014b, *MNRAS*, 445, 3073
 Park, D., Kelly, B. C., Woo, J.-H., & Treu, T. 2012, *ApJS*, 203, 6
 Parker, M. L., Wilkins, D. R., Fabian, A. C., et al. 2014, *MNRAS*, 443, 1723
 Patrick, A. R., Reeves, J. N., Porquet, D., et al. 2012, *MNRAS*, 426, 2522
 Perez, E., Robinson, A., & de La Fuente, L. 1992, *MNRAS*, 255, 502

Table 5. Inferred parameters for models *M1*, *M2*, and *M3*.

Parameter	<i>M1</i>	<i>M2</i>	<i>M3</i>
δ	$-0.17^{+0.10}_{-0.10}$	$-0.17^{+0.15}_{-0.13}$	$-0.11^{+0.13}_{-0.08}$
$\log(\mu/l_d)$	$0.92^{+0.31}_{-0.27}$...	$0.09^{+0.44}_{-0.66}$
β	$1.7^{+0.1}_{-0.1}$...	$1.5^{+0.3}_{-0.5}$
F	$0.09^{+0.02}_{-0.02}$...	$0.24^{+0.25}_{-0.21}$
$\log(\mu_l/l_d)$	$1.22^{+0.21}_{-0.39}$
β_l	$1.1^{+0.3}_{-0.2}$
F_l	$0.15^{+0.09}_{-0.05}$
ρ_l	$0.38^{+0.10}_{-0.10}$
α	...	$1.2^{+0.1}_{-0.1}$...
$\log(R_0/l_d)$...	$0.5^{+0.2}_{-0.4}$...
F_{in}	...	$0.10^{+0.11}_{-0.06}$...
$\log F_{out}$...	$0.99^{+0.01}_{-0.01}$...
θ_{inc} (degree)	45^{+10}_{-12}	37^{+10}_{-19}	41^{+21}_{-11}
θ_{opn} (degree)	36^{+10}_{-11}	43^{+11}_{-10}	30^{+14}_{-12}
$\theta_{opn,l}$ (degree)	10^{+26}_{-5}
κ	$-0.36^{+0.08}_{-0.09}$	$-0.48^{+0.04}_{-0.01}$	$-0.38^{+0.73}_{-0.09}$
γ	$4.44^{+0.4}_{-1.5}$	$4.3^{+0.5}_{-2.3}$	$3.7^{+0.8}_{-1.6}$
ξ	$0.06^{+0.10}_{-0.05}$	$0.18^{+0.09}_{-0.11}$	$0.33^{+0.52}_{-0.25}$
$\log(M_{\bullet}/M_{\odot})$	$5.90^{+0.31}_{-0.31}$	$6.34^{+0.37}_{-0.25}$	$6.23^{+0.26}_{-0.45}$
f_{ellip}	$0.02^{+0.04}_{-0.01}$	$0.01^{+0.02}_{-0.01}$	$0.10^{+0.28}_{-0.07}$
f_{flow}	$0.76^{+0.16}_{-0.20}$	$0.69^{+0.20}_{-0.28}$	$0.42^{+0.44}_{-0.24}$
$f_{ellip,l}$	$0.14^{+0.31}_{-0.12}$
$f_{flow,l}$	$0.56^{+0.32}_{-0.33}$
θ_e (degree)	19^{+13}_{-12}	5^{+9}_{-4}	27^{+26}_{-22}
σ_{turb}	$-2.2^{+0.7}_{-0.5}$	$-2.1^{+0.6}_{-0.5}$	$-2.0^{+0.6}_{-0.7}$

Perez, E., Robinson, A., & de La Fuente, L. 1992, MNRAS, 256, 103
Perry, J. J., van Groningen, E., & Wanders, I. 1994, MNRAS, 271, 561
Peterson, B. M. 1993, PASP, 105, 247
Peterson, B. M. 2014, SSRv, 183, 253
Peterson, B. M., Berlind, P., Bertram, R., et al. 2002, ApJ, 581, 197
Peterson, B. M., Ferrarese, L., Gilbert, K. M., et al. 2004, ApJ, 613, 682
Peterson, B. M., Grier, C. J., Horne, K., et al. 2014, ApJ, 795, 149
Peterson, B. M., & Wandel, A. 1999, ApJL, 521, L95
Peterson, B. M., Wanders, I., Bertram, R., et al. 1998, ApJ, 501, 82
Petrov, R. G., Millour, F., Lagarde, S., et al. 2012, Proc. SPIE, 8445, 84450W
Proga, D., Jiang, Y.-F., Davis, S. W., Stone, J. M., & Smith, D. 2014, ApJ, 780, 51
Rakshit, S., & Stalin, C. S. 2017, ApJ, 842, 96
Rakshit, S., Petrov, R. G., Meilland, A., & Hönig, S. F. 2015, MNRAS, 447, 2420
Rodríguez-Pascual, P. M., Alloin, D., Clavel, J., et al. 1997, ApJS, 110, 9
Rybicki, G. B., & Press, W. H. 1992, ApJ, 398, 169
Schwarz, G. E. 1978, Annals of Statistics, 6, 461
Shakura, N. I., & Sunyaev, R. A. 1973, A&A, 24, 337
Shen, Y., Greene, J. E., Strauss, M. A., Richards, G. T., & Schneider, D. P. 2008, ApJ, 680, 169

Sivia, D., & Skilling, D. 2006, Data Analysis: A Bayesian Tutorial (New York: Oxford Univ. Press)
Skjelboe, A., Pancoast, A., Treu, T., et al. 2015, MNRAS, 454, 144
Stern, J., Hennawi, J. F., & Pott, J.-U. 2015, ApJ, 804, 57
Véron-Cetty, M.-P., Véron, P., & Gonçalves, A. C. 2001, A&A, 372, 730
Vestergaard, M., & Osmer, P. S. 2009, ApJ, 699, 800
Walton, D. J., Nardini, E., Fabian, A. C., Gallo, L. C., & Reis, R. C. 2013, MNRAS, 428, 2901
Wandel, A. 1997, ApJL, 490, L131
Wanders, I. 1995, A&A, 296, 332
Wang, J.-M., Du, P., Baldwin, J. A., et al. 2012, ApJ, 746, 137
Wang, J.-M., Du, P., Hu, C., et al. 2014a, ApJ, 793, 108 (Paper II)
Wang, J.-M., Qiu, J., Du, P., & Ho, L. C. 2014b, ApJ, 797, 65
Wang, J.-M., & Zhou, Y.-Y. 1999, ApJ, 516, 420
Welsh, W. F. 1999, PASP, 111, 1347
Williams, P. R., Pancoast, A., Treu, T., et al. 2018, ApJ in press (arXiv:1809.05113)
Woo, J.-H., Schulze, A., Park, D., et al. 2013, ApJ, 772, 49
Xiao, M., Du, P., Horne, K., et al. 2018, ApJ, 864, 109 (Paper VII)
Zhou, H., Wang, T., Yuan, W., et al. 2006, ApJS, 166, 128
Zu, Y., Kochanek, C. S., Kozłowski, S., & Udalski, A. 2013, ApJ, 765, 106
Zu, Y., Kochanek, C. S., & Peterson, B. M. 2011, ApJ, 735, 80